Monthly Notices
of the
ROYAL ASTRONOMICAL SOCIETY

MNRAS **479,** 2630–2648 (2018)
Advance Access publication 2018 June 23

doi:10.1093/mnras/sty1666

Galaxy–galaxy lensing in the outskirts of CLASH clusters: constraints on local shear and testing mass–luminosity scaling relation

Guillaume Desprez,[1,2]★ Johan Richard,[2] Mathilde Jauzac,[3,4,5] Johany Martinez,[2] Brian Siana[6] and Benjamin Clément[2]

[1]*Department of Astronomy, University of Geneva, ch. d'Ecogia 16, CH-1290 Versoix, Switzerland*
[2]*Univ. Lyon, Univ. Lyon1, Ens de Lyon, CNRS, Centre de Recherche Astrophysique de Lyon UMR5574, F-69230 Saint-Genis-Laval, France*
[3]*Centre for Extragalactic Astronomy, Department of Physics, Durham University, Durham DH1 3LE, UK*
[4]*Institute for Computational Cosmology, Durham University, South Road, Durham DH1 3LE, UK*
[5]*Astrophysics and Cosmology Research Unit, School of Mathematical Sciences, University of KwaZulu-Natal, Durban 4041, South Africa*
[6]*Department of Physics and Astronomy, University of California, Riverside, CA 92521, USA*

Accepted 2018 June 20. Received 2018 June 18; in original form 2018 April 18

ABSTRACT

We present a selection of 24 candidate galaxy–galaxy lensing (GGL) identified from *Hubble* images in the outskirts of the massive galaxy clusters from the Cluster Lensing And Supernova survey with Hubble (CLASH) . These GGLs provide insights into the mass distributions at larger scales than the strong-lensing region in the cluster cores. We built parametric mass models for three of these GGLs showing simple lensing configurations, in order to assess the properties of their lens and its environment. We show that the local shear estimated from the GGLs traces the gravitational potential of the clusters at a radial distance of 1–2 arcmin, allowing us to derive their velocity dispersion. We also find a good agreement between the strength of the shear measured at the GGL positions through strong-lensing modelling and the value derived independently from a weak-lensing analysis of the background sources. Overall, we show the advantages of using single GGL events in the outskirts of clusters to robustly constrain the local shear, even when only photometric redshift estimates are known for the source. We argue that the mass–luminosity scaling relation of cluster members can be tested by modelling the GGLs found around them, and show that the mass parameters can vary up to ∼30 per cent between the cluster and GGL models assuming this scaling relation.

Key words: gravitational lensing: strong – gravitational lensing: weak – galaxies: clusters: general – galaxies: clusters: individual: MACS J1149 – galaxies: clusters: individual: MACS J0329 – galaxies: clusters: individual: RX J2129.

1 INTRODUCTION

Dark matter (DM) is one of the most challenging questions in modern astrophysics. It is indeed the most common matter species in the Universe according to the most commonly accepted model of cosmology, Λ cold dark matter (ΛCDM), but remains undetectable directly. Its abundance in the largest observable structures of the Universe, such as galaxy clusters and massive galaxies, makes these systems ideal probes to understand its properties.

Galaxy clusters are the most massive collapsed objects observable, and their matter content is dominated by DM (up to ∼85 per cent). Due to their high mass, they will act as gravitational lenses, deflecting the light coming from galaxies located behind (see Massey, Kitching & Richard 2010; Kneib & Natarajan 2011; Hoekstra et al. 2013, for some reviews). The geometry and location of these deflected images of background galaxies can be used to trace the DM distribution in these clusters. In the core of clusters where the density is the highest, we observe highly magnified and multiple images of background galaxies, this is the strong-lensing regime (Soucail et al. 1988). However, even for the most massive and concentrated cluster cores, the strong-lensing region remains small, up to ∼20–40 arcsec (typically <500 kpc) from the cluster centre (Richard et al. 2010a; Merten et al. 2011; Zitrin et al. 2011; Richard et al. 2014; Grillo et al. 2015; Jauzac et al. 2015). Extending outside this region, the density drops and the distortions are much smaller, this is the weak-lensing regime (Smith et al. 2005; Jauzac et al. 2012; Medezinski et al. 2013; Umetsu et al. 2015). By combining both lensing regimes, we can trace the mass distribution of galaxy clusters up to a few Mpc radius (Bradač et al. 2005; Limousin et al. 2007; Jauzac et al. 2015, 2016, 2017).

★ E-mail: guillaume.desprez@unige.ch

Another effect of the high mass density of galaxy clusters at large radii is to boost the strong-lensing cross-section of individual galaxies (in particular the ones at or around the cluster redshift), increasing the number of galaxy–galaxy lensing (GGL). Indeed, Limousin et al. (2007) identified three such lenses within 2 arcmin of the core of the massive cluster Abell 1689, compared to the much lower probability of occurrence of GGL in blank fields (e.g. 10 deg^{-2}, Faure et al. 2008).

The presence of a massive galaxy cluster will locally affect the observed positions of multiple images in a GGL system. Perturbed GGLs are a sign of the effect of the lens environment (Limousin et al. 2010). Tu et al. (2008) demonstrated how GGL events in cluster fields can be used as direct probes of the radial slope of the cluster density profile (up to ∼400-kpc radius). The Cluster Lensing And Supernova survey with Hubble (CLASH, Postman et al. 2012) observed a sample of 25 massive galaxy clusters with the *Hubble Space Telescope* (*HST*), from the ultraviolet (UV) to the near-infrared (NIR), to study their gravitational lensing properties. This combination of the high-resolution from space with information on colours is perfectly suited to identify GGLs in the cluster outskirts.

In this paper, we present a catalogue of candidate GGLs selected in all CLASH fields through visual inspection of the *Hubble* images. We perform strong-lensing mass reconstructions for three of them, detected in the RX J2129, MACS J0329, and MACS J1149 clusters, suitable to probe the cluster mass profiles at large radii, i.e. outside the strong-lensing region, and for which redshift estimates for the lenses and the sources are available. The paper is organized as follows: In Section 2, we detail the GGL sample selection and the observations at hand; in Section 3, we present our modelling and results for three GGLs; in Section 4, we discuss our results and put them in perspective, e.g. GGL measurements relative to weak-lensing measurements.

Throughout the paper, we give the magnitudes in the AB system and assume the standard ΛCDM model with the following cosmology: $\Omega_m = 0.3$, $\Omega_\Lambda = 0.7$, and $H_0 = 70\,\mathrm{km\,s^{-1}\,Mpc^{-1}}$.

2 OBSERVATIONS AND SAMPLE SELECTION

We present here the observations and data sets used for our analysis. The identification of GGLs is based on the inspection of high-resolution *HST* images from the CLASH programme.

2.1 Photometric data and GGL selection

2.1.1 HST *imaging data*

Each cluster was observed with *HST* in 16 pass-bands, from UV (∼200 nm) to NIR (∼1600 nm) using the Wide Field Camera 3 (WFC3) UVIS/IR and the Advanced Camera for Survey (ACS). We used the publicly released CLASH images with a pixel scale of 30 mas retrieved from the MAST archive.[1] In the case of MACS J0416, MACS J0717, MACS J1149, and AS 1063, we used *HST* images obtained with the Hubble Frontier Fields (HFF) programme (Lotz et al. 2017),[2] as they supersede the CLASH images in depth near the cluster centre.

[1] https://archive.stsci.edu/missions/hlsp/clash/
[2] https://archive.stsci.edu/missions/hlsp/frontier/

2.1.2 GGL identification

Several dedicated codes have been developed to perform an automatic detection of gravitational arcs and arclets in wide-field images (e.g. ARCFINDER and YATTALENS; Seidel & Bartelmann 2007; Sonnenfeld et al. 2017). Because of the small number of clusters with high-resolution imaging, we preferred to use visual inspection instead. This gives us more flexibility to extend the search in the outskirts of the images where the sky coverage varies from filter to filter. More importantly, we do not focus on a specific lensing configuration (Einstein ring or giant arc) as for the majority of automatic detection codes, and include compact (unresolved) images as well. This visual inspection is not an issue as the completeness of our sample is not necessary for our study.

We focus our search on bright galaxies in the outskirts of the clusters for which strong-lensing models of the cores are available (e.g. Ebeling et al. 2009; Richard et al. 2011; Zitrin et al. 2012, 2015). Candidate GGLs were selected in combined-colour images of the clusters using the (*F*475*W*–*F*606*W*–*F*850*LP*) filter combination, or (*F*435*W*–*F*606*W*–*F*814*W*) when HFF images are being used. We also make use of the NIR bands (*F*606*W*–*F*105*W*–*F*160*W*) at the cluster cores. The selection is based on the similarity in colour, morphology, and position of the lensed images around bright galaxies. All the GGL candidates are then carefully examined in all *HST* bands in which they appear, to confirm or discard the strong-lensing hypothesis. A selection of 24 GGL candidates is presented in Table A1 and Fig. A1. Unsurprisingly, our selection detects well-known GGLs. For example, the *Dragon Kick* from Diego et al. (2015) or the system *ID14* from Vanzella et al. (2017) in MACS J0416.

Considering the importance of GGL events in the outskirts of the clusters, we choose to focus for the rest of the paper on the most interesting GGLs satisfying the following selection criteria:

(i) an angular separation from the BCG larger than 80 arcsec ;
(ii) plausible lensing configuration from visual inspection (having noticeable multiple images well separated from the lens);
(iii) single, bright galaxy lenses that do not belong to a galaxy group.

This selection provides us with three GGL candidates highlighted in the bottom panel of Fig. 1, with their characteristics listed in Table 1:

(i) RX J2129−GGL1 is being quadruply lensed by an elliptical galaxy. Its four extended multiple images are seen to spiral around the lens. This elliptical and spiral-like configuration led us to refer to it as the *Snail*.
(ii) MACS J0329−GGL1 is a system surrounding a central elliptical galaxy. It consists of an extended arc to the east and a smaller arc to the west. We note that the distances of the two arcs from the lens are unusually different. The colours of the arcs components being the same suggest that there is a single background source.
(iii) MACS J1149−GGL1 is being lensed by an elliptical galaxy, and forms an almost perfect Einstein cross: The four images are nearly symmetric with a small angle from a perfectly perpendicular cross.

2.1.3 Deblending

The lens and multiple images in MACS J0329−GGL1 and MACS J1149−GGL1 are well-separated. However, in the case of RX J2129−GGL1, the lens is contaminating the source. In order to

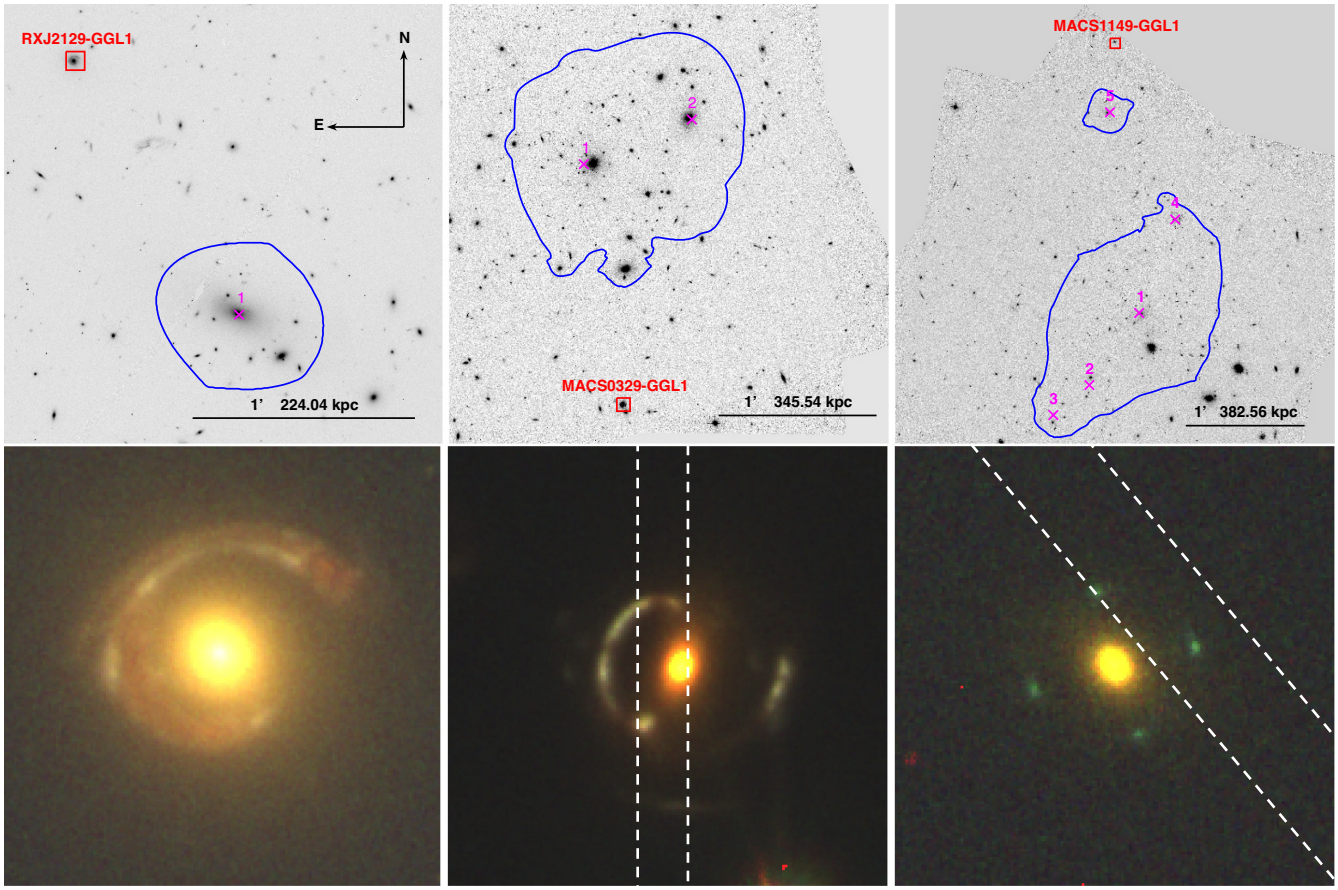

Figure 1. *HST* images of the three clusters hosting the three GGL candidates that are at the core of this paper. Top panel: a view of the clusters in the *F*775*W* band. The location of the GGL in each cluster is highlighted with a red box. The blue contours delineate the multiple image regions expected for sources at $z = 6$. Bottom panel (from the left- to right-hand side): RX J2129−GGL1 (a.k.a the *Snail*), MACS J0329−GGL1, and MACS J1149−GGL1. The images are 5×5 arcsec^2. For the first two images, the blue channel combines *F*435*W* and *F*475*W* filters, the green one combines *F*606*W* and *F*625*W*, and the red one combines the *F*775*W*, *F*814*W*, and *F*850*LP* bands. For the third stamp, *F*435*W*, *F*606*W*, and *F*775*W* are being used for the blue, green, and red channels, respectively. North is up and east is left. The dashed white lines in the bottom middle and right-hand panels indicate the slit positioning for the spectroscopy.

Table 1. The three GGLs selected in this study. From the left- to right-hand columns: ID, coordinates (J2000) of the centre of the lens, redshift of the cluster, galaxy lens, and source, distance to the BCG, and the magnitude measured in the *F*775*W* band of the lens and the source.

ID	α	δ	z_c	z_l	z_s	d_{BCG} (arcsec)	*F*775*W* (mag)	Source *F*775*W* (mag)*
RX J2129−GGL1	322.4287798	0.1080707	0.235	$0.255^{+0.033a}_{-0.021}$	$1.61^{+0.37a}_{-0.31}$	81.0	17.58 ± 0.01	21.02 ± 0.04
MACS J0329−GGL1	52.4201304	−2.2216321	0.45	0.3835^b	1.112^b	92.0	19.59 ± 0.01	19.88 ± 0.01
MACS J1149−GGL1	177.40.28.221	22.43.66292	0.544	0.542^b	1.806^b	137.9	20.22 ± 0.06	22.52 ± 0.02

[a]photometric redshift with a 2σ error (Section 2.2.2).
[b]Spectroscopic redshift (Section 2.2.1).
*Observed magnitude.

obtained a precise photometry, we modelled the lens and subtracted it from the image, using the GALFIT (Peng et al. 2011) software.

The input files are first generated by GALAPAGOS (Barden et al. 2012). We then manually define the input mask to reject all pixels belonging to the source (blue contour shown in the left panel of Fig. 2) in the modelling of the lens. GALFIT fits the lens with a Sérsic profile using the eight different available pass-bands between *F*390*W* and *F*850*LP* (Table 2) where the lens is fully detected. During the modelling, parameters such as position (x, y) and shape (radius, axis ratio and position angle) are assumed to be constant with wavelength. The Sérsic index can linearly evolve with wavelength, and the magnitude is considered as a free parameter. The residual image is shown in the right-hand panel of Fig. 2.

2.1.4 Photometry

Photometric catalogues are publicly available for all CLASH clusters as part of the delivered high-level science products,[3] providing positions, shapes, magnitudes, and photometric redshifts of the ex-

[3]https://archive.stsci.edu/missions/hlsp/clash/

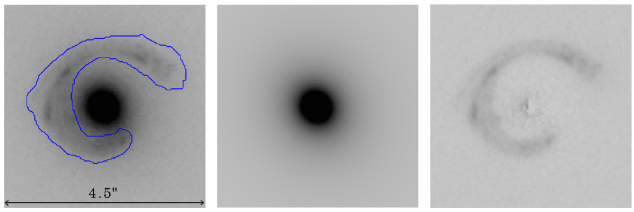

Figure 2. Deblending method on RX J2129−GGL1. Left-hand panel: the initial image as seen in the *F*814*W* band. The blue contour highlights the shape used for the mask (see Section 2.1.3), and also used for the aperture photometry (see Section 2.1.4). Middle panel: the Sérsic model of the lens fitted by GALFIT. Right-hand panel: the residual image.

tracted objects. These catalogues are used to derive the photometry in MACS J0329−GGL1.

None of the lensed images in MACS J1149−GGL1 multiple images is detected in this catalogue. We used SEXTRACTOR (Bertin & Arnouts 1996) in order to get a clean photometry for these images in all the bands where the GGL appears (*F*435*W*, *F*606*W*, *F*625*W*, and *F*775*W*). The combined *F*775*W*-band magnitude is provided in Table 1.

To measure the source magnitudes for RX J2129−GGL1, we use the residual image presented in Section 2.1.3 (right-hand panel of Fig. 2). Due to the complex morphology of this source, we use the manually defined aperture (blue contours in Fig. 2) to measure the source flux, and then remove the background previously estimated in an outer annulus (2.1–2.4 arcsec). In the case of the lens, we use GALFIT to fit a Sérsic profile to the lens and get the magnitudes, a mask to hide the source flux has been applied. Magnitudes measured by GALFIT are listed in Tables 1 and 2 .

For the modelling part detailed in Section 3, we need the geometrical parameters (centroid, α_c and δ_c, ellipticity, e_c, position angle, θ_c) and the luminosity of the cluster members. For MACS J1149 and RX J2129, we use the galaxy catalogues from Jauzac et al. (2016) and Richard et al. (2010b), respectively. We incorporate the photometry of the new CLASH images in the RX J2129 catalogue, using the *F*160*W* band. For the galaxies not appearing in the WFC3 field of view, we use ACS/*F*814*W* and apply a mean (*F*160*W*–*F*814*W*) colour estimated with the Coleman, Wu & Weedman (1980) empirical template for elliptical galaxies. We also use the geometrical parameters (α_c, δ_c, e_c, θ_c) measured in the *F*814*W* band for the RX J2129 cluster members catalogue.

In the case of MACS J0329, we select the cluster members following the red-sequence technique on a (*F*606*W*-*F*814*W*) versus *F*814*W* colour–magnitude diagram. We chose a limiting magnitude *F*814*W* = 23 and a colour width of 0.3 mag for the red sequence (above three times the photometric uncertainties). We incorporate the *F*160*W* photometry when galaxies are visible in this pass-bands. Finally, we add the geometrical parameters (α_c, δ_c, e_c, θ_c) measured in the *F*814*W* band to the catalogue.

2.2 Redshift estimates

2.2.1 Spectroscopic redshift

All CLASH clusters have been extensively covered with the VIsible MultiObject Spectrograph (VIMOS, Le Fèvre et al. 2003) on the Very Large Telescope, as part of the ESO programme 186.A-0798 (PI: Rosati, Rosati et al. 2014). We looked at all the masks covering the three studied clusters and found that MACS J0329−GGL1 had been targeted for one 1125-s exposure obtained with the medium-resolution ($R = 580$) grism during the night of 2012 December 1. The slit position is presented in the bottom middle panel of Fig 1.

The spectra were extracted using the VIMOS pipeline v2.9.16. Following the instruction in the manual v6.8,[4] we performed standard reduction with the new recipes for bias removal, flat-field correction, wavelength calibration, sky subtraction, and used observations of spectroscopic standard stars to derive the flux calibration.

The extracted spectrum of the galaxy in the medium resolution grism is presented in Fig. 3. We identify the presence of K, H, G, and NaD absorption lines and a Balmer break at a redshift $z_l = 0.3835$. We also note an emission line that does not match the lens redshift. We identify it as an [O II] emission line belonging to the source at redshift $z_s = 1.112$. This redshift is consistent with additional absorption lines of Mg II in the continuum.

A spectrum of the western image of MACS J1149−GGL1 was obtained with the LRIS instrument (Oke et al. 1995; Steidel et al. 2004) on the Keck I telescope. The position angle was 40° and the slit width was 1.0 arcsec (see Fig 1) and the airmass ranged from 1.03 to 1.12. Three exposures of 27 min each were taken for a total exposure time of 81 min.

The extracted spectrum is presented in Fig. 4. Spectral features are detected from both the lens and background source. Strong Ly α is found in emission at $\lambda = 3410$ Å, corresponding to a redshift $z_s = 1.806$. In the red part of the spectrum, we observe K and H absorption lines of the lens galaxy (not centred in the slit) at wavelengths of 6066 and 6120 Å, respectively. This corresponds to a redshift $z_l = 0.542$ for the lens, in agreement with the cluster redshift.

2.2.2 Photometric redshifts

For the RX J2129−GGL1 system, we used HYPERZ (Bolzonella, Miralles & Pelló 2011) to fit the spectral energy distribution (SED) and estimate photometric redshifts for the lens and the source. To fit the SED, we used models made from Bruzual & Charlot (2003) with an initial mass function from Salpeter (1955) and a metallicity of 0.02 $Z_\odot$, and with the reddening law of Calzetti et al. (2000), we allowed AV to be in the range [0.0–3.0]. HYPERZ provides the probability distribution of the photometric redshift of the system. It shows three maxima at $z = 1.1$, 1.6, and 2.4 (Fig. 5).

Based on the physical parameters derived on the lens during our modelling (Section 3), the redshift solution $z = 1.6$ is preferred, and is given with its associated error in Table 1. We discuss this assumption later in Section 4.2.1.

3 MODELS

We build parametric models of the mass distribution of the GGLs in order to reproduce the observed lensing configurations. Models have varying complexity in order to test different assumptions of the impact of the environment. The same methodology was applied to each GGL for constructing the models and analysing the results.

3.1 Methodology

We use the software LENSTOOL (Kneib 1993; Jullo et al. 2007) to optimize parametric models of the mass distribution in each system. LENSTOOL uses the observed positions of multiple images as constraints. For a set of mass parameters and a given system of

[4] ftp://ftp.eso.org/pub/dfs/pipelines/vimos/vimos-pipeline-manual-6.8.pdf

Table 2. Photometry for the GGL of RX J2129 in all the available bands and the computed photo-z.

ID	*F390W*	*F435W*	*F475W*	*F606W*	*F625W*	*F775W*	*F814W*	*F850LP*	Photo-z
RX J2129									
Lens	20.55 ± 0.01	20.10 ± 0.01	19.41 ± 0.01	18.26 ± 0.01	18.05 ± 0.01	17.58 ± 0.01	17.50 ± 0.01	17.24 ± 0.01	$0.245^{+0.086}_{-0.019}$
Source[a]	22.86 ± 0.12	22.48 ± 0.07	22.27 ± 0.07	21.78 ± 0.02	21.61 ± 0.03	21.02 ± 0.04	20.79 ± 0.03	20.32 ± 0.02	1.61^{+}_{-}

Note: [a]Photometry combines all multiple images together.

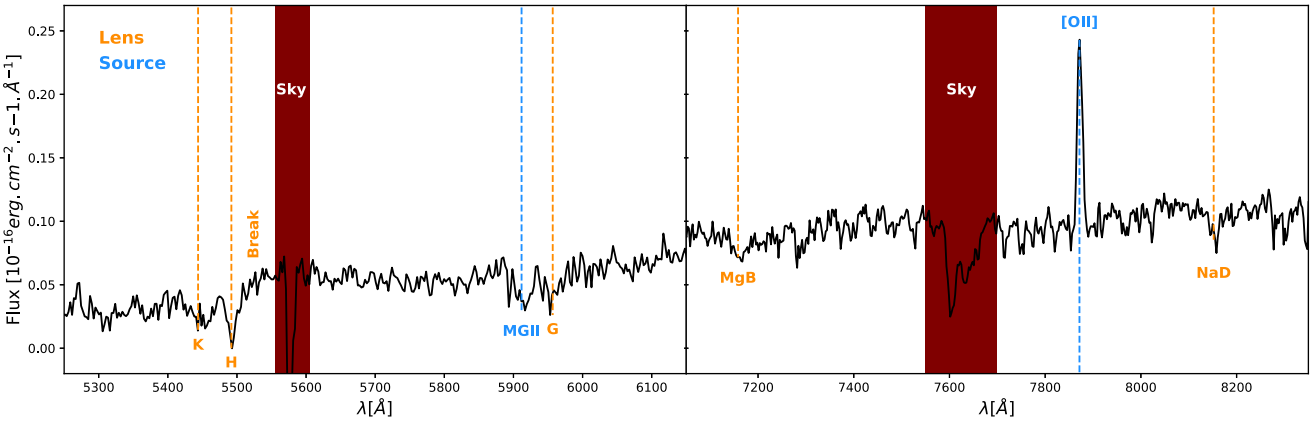

Figure 3. VIMOS extracted spectrum of both MACS J0329−GGL1 lens and source. In orange, the lines of the lens with a redshift $z_l = 0.3835$, and in blue, the line of the source with a redshift $z_s = 1.112$. We identify the K, H, G MgB, and NaD absorption lines for the lens and its Balmer break. For the source, we observe the [O II] emission lines and the Mg II absorption lines.

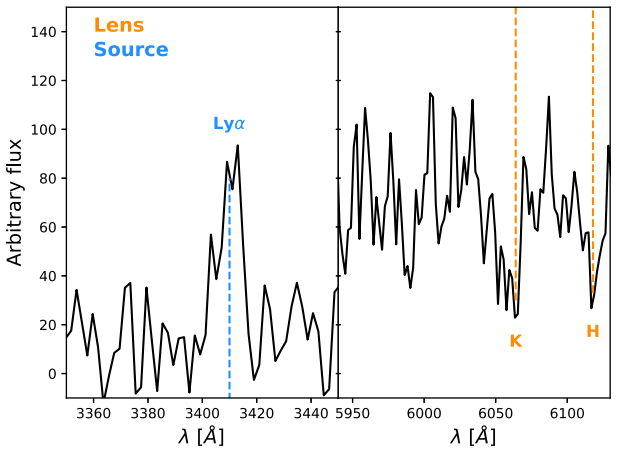

Figure 4. Spectrum of the MACS J1149 GGL. A Ly α emission is detected at $\lambda = 3410$ Å from the background source. Ca absorption lines from the lens are present at $\lambda_K = 6066$ Å and $\lambda_H = 6120$ Å, at the edge of the LRIS blue arm spectral coverage. This corresponds to $z_s = 1.806$ and $z_l = 0.542$, respectively.

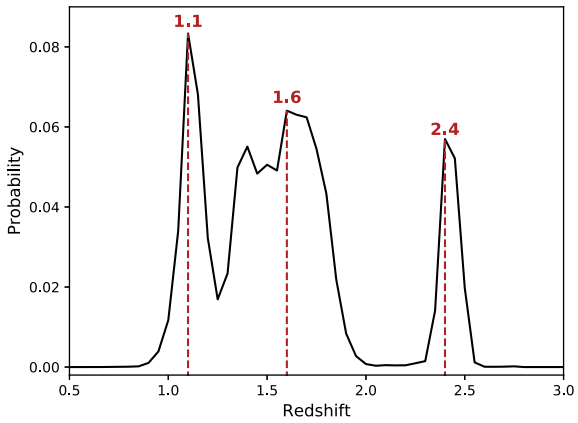

Figure 5. Probability density function of t he Snail source photometric redshift. We note three maxima, located at redshift $z = 1.1$, 1.6 2.4.

multiple images, it computes the barycentre of all positions in the *source* plane. It then lenses this location back into the *image* plane. The model parameters are sampled using a Markov chain Monte Carlo (MCMC) and optimized through a χ^2 minimization using the distances between the observed and model-predicted positions of the multiple images.

The three GGLs are dominated by a massive central galaxy lens. The mass distribution of the lens galaxy is usually well described with a single parametric potential, but the effect of its (generally unknown) environment is included in the form of a constant external shear field (Schechter et al. 1997; Dye et al. 2007; Wagner & Bartelmann 2016; Wong et al. 2017). Here, we know that the environment of each GGL is certainly dominated by the nearby massive galaxy cluster.

The mass distribution is modelled by a superposition of mass components describing galaxy- and/or cluster-scales. These gravitational potentials are described by double Pseudo-Isothermal Elliptical (dPIE) profiles (Elíasdóttir et al. 2007). This distribution is described by the following parameters:

(i) the geometrical parameters (central position α_c, δ_c, ellipticity and position angle e_c, θ_c);
(ii) the central velocity dispersion, σ_0;
(iii) a cut radius, r_{cut};
(iv) a core radius, r_{core}.

Four models are constructed for a given GGL, each model getting a higher level of complexity than the previous depending on the assumption used on the environment. We start by only modelling

the single central galaxy lens, and, finally, the whole cluster and GGL are constrained together.

We adjust for each model the parameters to optimize and the range of values. The results presented in this work are the best models, with the lowest χ^2, with the parameters presented in Appendix B.

Model I: single galaxy lens. In this model, we only consider the lens of the GGL as the deflector, ignoring the effect from other lenses. Only the σ_0 of the mass component is optimized, its ellipticity and position angle are set to the ones of the light measured in Section 2.1.4. Due to its degeneracy with σ_0 (Richard et al. 2010b), $r_{\rm cut}$ is fixed to a typical value of 50 kpc. This hypothesis is further discussed in Section 4.1. $r_{\rm core}$ is fixed to 0 as it does not have an impact on the lensing effect.

Model II: single galaxy lens and external shear. In this model, we use the same parametrization as model I for the galaxy, and assume the lensing contribution of the environment surrounding the GGL is well modelled by adding a constant external shear. The magnitude γ of this shear and its orientation θ are free additional parameters like σ_0 of the lens. The shear magnitude is given for a $D_{\rm LS}/D_{\rm OS}$, ratio of angular distances between the lens and the source and between the observer and the source, respectively, equal to 1.

Model III: cluster and GGL. This model includes a full optimization of the cluster and the GGL system. Cluster size potentials are being optimized with a fixed $r_{\rm cut} = 1000$ kpc, but their position, σ_0, ellipticity, position angle, and $r_{\rm core}$ are free to vary. The BCG as well as the lens of the GGL system are being modelled by a dPIE potential, setting σ_0 as a free parameter.

With a sufficient number of constraints, the $r_{\rm cut}$ of the BCG can be optimized. Cluster members are being modelled by individual galaxy-size potentials, but to limit the number of parameters we assume they follow the Faber–Jackson scaling-relation (Faber & Jackson 1976) as described in Richard et al. (2010b):

$$\sigma_0 = \sigma_0^* \left(\frac{L_{F160W}}{L^*_{F160W}}\right)^{1/4}, \quad (1)$$

$$r_{\rm cut} = r^*_{\rm cut} \left(\frac{L_{F160W}}{L^*_{F160W}}\right)^{1/2}, \quad (2)$$

$$r_{\rm core} = r^*_{\rm core} \left(\frac{L_{F160W}}{L^*_{F160W}}\right)^{1/2}. \quad (3)$$

This relation links the $F160W$-band luminosity, L_{F160W}, to a L^*_{F160W}, and scales the mass parameters of the cluster members to the ones of the standard galaxy (σ_0^*, $r^*_{\rm cut}$, $r^*_{\rm core}$). The luminosity of the standard galaxy is computed following the results of Lin et al. (2006) as in the work of Richard et al. (2010b). We optimize σ_0^* and fix $r^*_{\rm cut}$ at 45 kpc and $r^*_{\rm core}$ at 0.15 kpc.

All the multiple image systems are included as constraints to this model. In the case of an unknown redshift of the source, the redshift is included as a free parameter of the model.

Model IV: cluster only. This model is similar to the previous one, but the GGL multiple images are not used to constrain the model. The lens of the GGL, when in the cluster, is included and assumed to follow the scaling relation described before. We use this model as a point of comparison with the model III to estimate the impact of the GGL constraints on the cluster mass distribution.

Analysis of the results. For the models I, II, and III, we use as a comparison parameter the root mean square (rms) of the distance between the observed and predicted position of the multiple images. The rms for all three clusters and models is listed in Table 3, and further discussed in Section 4.

Table 3. rms of the predicted positions of the multiple images of the GGLs systems with the different models, given in arcsec.

Cluster ID	Model I (arcsec)	Model II (arcsec)	Model III (arcsec)
MACS0329	0.20	0.07	0.10
MACS1149	0.26	0.07	0.17
RX J2129	0.66	0.02	0.03

We also compare the produced shear by the models II, III, and IV. The result of the shear optimization is scaled with the $D_{\rm LS}/D_{\rm OS}$ factor of the GGL for the model II. For the two others, the shear is measured by making a shear map at the position of the GGL after subtracting it from the models. We construct 5×5 arcmin^2 maps of 50 pixels across for the two components of the shear, γ_1 and γ_2 ($\gamma \equiv \gamma_1 + {\rm i}\gamma_2$; see Bartelmann & Schneider 2001). We then measure their mean values.

From these values of γ_1 and γ_2, we then compute the magnitude and the orientation of the shear. We apply the same methodology to all the realizations of each model. We can then measure the scatter in both shear magnitude and orientation. To compute contours containing 68.3and 95.4 per cent of all the points, we used a Gaussian kernel density estimation with a bandwidth selected using Scott's (1992) rule of thumb. The results produced are contour maps of the shear versus its orientation (see Figs 7, 9, and 11).

3.2 RX J2129

Our model of RX J2129 ($z_{\rm c} = 0.235$) is based on the one presented by Richard et al. (2010b). This model includes 39 cluster galaxies, comprising both the BCG and the central galaxy lens in RX J2129−GGL1. Richard et al. (2010b) used a triply imaged system near the BCG with a known spectroscopic redshift, $z = 1.965$. Since then, this redshift has been revised to $z = 1.522$ (Belli et al. 2013). We include in our model two multiply-imaged systems from Zitrin et al. (2015): systems #3 and #5. For system #5, we use only images 1 and 2. For both systems, the redshift is included as a free parameter.

The *Snail* is a GGL located north-east of RX J2129 core, at a distance of 81 arcsec from the BCG (see Fig. 1, Table 1). As the image in Fig. 1 shows, one can see four multiple images around the central elliptical galaxy. Their positions are listed in Table B1. We note that all images are close to the lens, leading to a contaminated photometry. That problem can be solved by subtracting the central galaxy in all the bands and is discussed in Section 2.1.3.

The photometry of the images after subtraction is given in Table 2. The photometry of the source is measured trough an aperture that is covering all the multiple images (see Fig. 2). We use that photometric catalogue to compute a photometric redshift for both the lens and the source. In Richard et al. (2010b), the *Snail* was considered as a cluster member, the photometric redshift was measured at $z = 0.255^{+0.033}_{-0.021}$, consistent within the error bars to the one of the cluster $z_{\rm c} = 0.235$.

We can also note from the illustration of Fig. 1 that the ring of multiple images is being sheared. This shear seems to be perpendicular to the direction of the BCG (see Fig. 16). The best-fitting parameters for all RX J2129 models are given in Table B2.

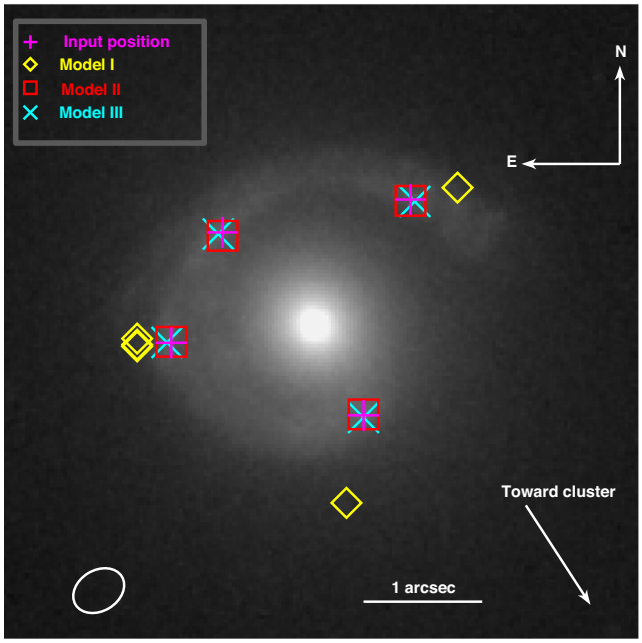

Figure 6. Predicted positions of the multiple image for all models for RX J2129−GGL1. Magenta crosses are the observed positions, yellow diamonds are the predictions from model I, red boxes are the predictions from model II with the external shear, and the cyan crosses are the predictions from model III, which includes the cluster. The white ellipse (lower left-hand corner) is the representation of the external shear on a circle of radius 0.2 arcsec.

Table 4. Table of the observed direction angle from the GGLs towards the BCGs and the computed angle from the perpendicular direction of the shear from models II. The last column is the velocity dispersion of an SIS at the position of the BCG derived from the shear magnitude. The error of θ_{obs} is the result to the propagation assuming a positional error of 0.5 arcsec for the BCG and the GGLs.

ID	θ_{obs} (°)	θ_{Mod} (°)	σ_{SIS} (km s^{-1})
RX J2129	-57.0 ± 0.36	$-58.5^{+3.3}_{-3.2}$	912^{+105}_{-70}
MACS0329	97.0 ± 0.32	$94.0^{+11.3}_{-2.1}$	1041^{+222}_{-131}
MACS1149	-83.3 ± 0.21	$-83.2^{+10.9}_{-4.7}$	1198^{+349}_{-172}

3.2.1 Model I

The lens of RX J2129−GGL1 was already included in the cluster scaling relations by Richard et al. (2010b). When modelling the GGL with a single galaxy potential, we fix its r_{core} to 0 kpc and r_{cut} to 64 kpc.

The best-fitting model predicts the images as they are presented in Fig. 6 (yellow diamonds) with an rms of 0.66 arcsec (Table 3). The image at the north of the *Snail* is not computed, and two images are predicted on the east. Also, the images are all predicted at a similar distance to the lens, indicating a ring-like configuration instead of the observed elliptical configuration. We thus conclude that a single galaxy lens is not sufficient to recover the observed configuration.

3.2.2 Model II

The predicted positions of the multiple images when considering an external shear are shown in Fig. 6 (red squares). They are in much better agreement with the observed ones as shown by an rms of 0.02 arcsec (see Table 3). The best model gives an external shear of amplitude $\gamma = 0.15^{+0.04}_{-0.03}$, and angle from the west direction of $\theta = 31.5^{+3.3}_{-3.2}$. That orientation is consistent with the direction towards the centre of the cluster with the BCG being oriented perpendicular to the predicted shear (see Table 4).

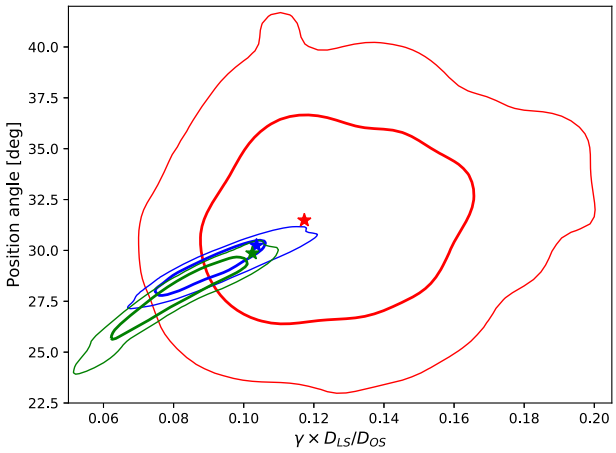

Figure 7. Predicted shear at the position of the *Snail* versus its orientation: in red the external shear predictions (model II), in green the predictions of the cluster-only model (model IV), and in blue the predictions from model III. The bold contour represents the 1σ limit and the thin one represents the 2σ. The stars show the best predictions for each model. The D_{LS}/D_{OS} factor is the one of the GGL.

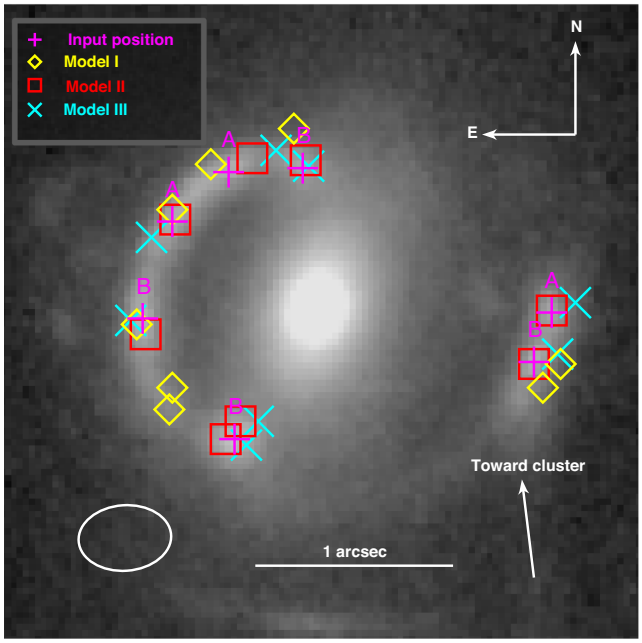

Figure 8. Same as Fig. 6 for MACS J0329−GGL1.

3.2.3 Model III

Here, we model both the *Snail* and the cluster. As in Richard et al. (2010b), each cluster galaxies, excepted for the *Snail* lens and the BCG, are modelled by a dPIE potential and following the Faber & Jackson (1976) scaling relation. The *K*-band luminosity was used to scale the parameters of the cluster members. We, thus, convert

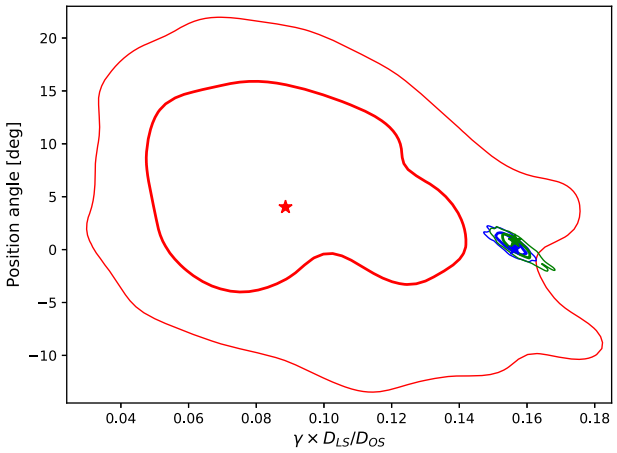

Figure 9. Same as Fig. 7 for MACS J0329 models.

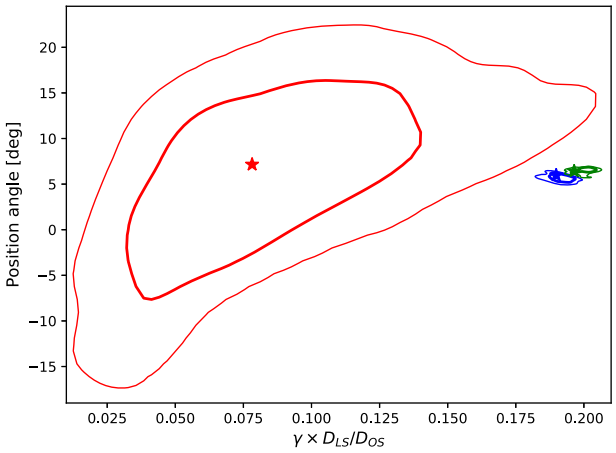

Figure 11. Same as Fig. 7 for MACS J1149 models.

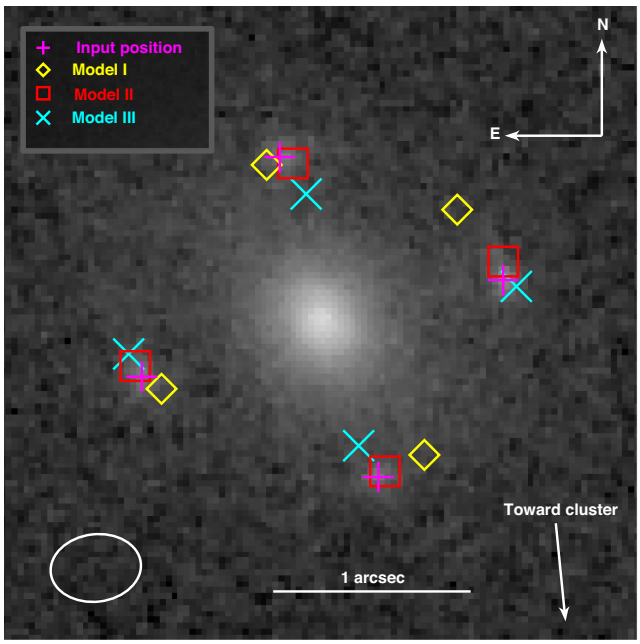

Figure 10. Same as Fig. 6. for MACS J1149−GGL1.

the L_K^* to L_{F160W}^* to scale the parameters with the $F160W$-band CLASH magnitudes, leading to $m_{F160W}^* = 17.49$. Finally, only the σ_0^* of the reference galaxy is optimized. The BCG and the *Snail* lens are being optimized individually, and only σ_0 is set as a free parameter.

To model the influence of the cluster at large radii, we create a PIEMD halo with a $r_{\rm cut} = 1000$ kpc. LENSTOOL optimizes the position of this halo in a box of 5 arcsec centred around the BCG, its orientation, ellipticity, $r_{\rm core}$ and σ_0.

We use as constraints all the multiple images presented in Table B1. For systems #3 and #5, we optimize the redshift and only use the positions of the multiple images as constraints. The best-fitting model gives $z_{s3} = 1.49^{+0.17}_{-0.09}$ and $z_{s5} = 0.78^{+0.05}_{-0.03}$. These results are within the 95 per cent confidence interval presented by Zitrin et al. (2015).

The predicted positions of the *Snail* are similar to the one obtained with model II (with an external shear). The resulting rms is 0.03 arcsec versus 0.02 arcsec for model II. Fig. 6 shows the predicted positions of the multiple images as cyan crosses. In Fig. 7, one can see the shear produced by the cluster in this model. The predicted shear from the cluster itself is close in orientation and intensity to the external shear obtained with model II.

3.2.4 *Model IV*

The lens of the RX J2129−GGL1 is treated in this model as a cluster member and optimized through the scaling relation. The GGL lens being at the edge of the *HST*/WFC3 field of view, its photometry in the $F160W$ band is computed as explained in Section 2.1.4.

The best-fitting model predicts a redshift of $z_{s3} = 1.55^{+0.17}_{-0.11}$ and $z_{s5} = 0.79^{+0.05}_{-0.04}$ for system #3 and #5, respectively. These results are close to the ones from model III. Fig. 7 shows the shear prediction at the position of the *Snail*. We note that the contours predicted by models III and IV are similar, but the one including the GGL constraints tend to be in better agreement with the predictions from the external shear model. The main difference between models III and IV is the value of the σ_0 predicted for the GGL lens. With the scaling relation and the values obtained for the standard galaxy, the GGLs lens is predicted to have $\sigma_0 = 114^{+26}_{-26}$ km s^{-1} in model IV, which differs from the value obtained with model III, $\sigma_0 = 179^{+3}_{-4}$ km s^{-1}.

3.3 MACS J0329

The model of MACS J0329 ($z_c = 0.45$) includes 177 cluster members plus the BCG and two cluster-scale haloes for which the positions are shown in Fig. 1. Following Zitrin et al. (2012), the model is constrained by three multiple image systems (Table B5), systems #1, #2, and #3. The redshift of system #1 is fixed to the well-constrained photometric redshift $z_{s1} = 6.18$. Zitrin et al. (2015) gives a spectroscopic redshift for system #2, $z_{s2} = 2.14$. The redshift of system #3 is included as a free parameters in our model.

The GGL found in MACS J0329 is located to the south of the cluster. It is separated by 92 arcsec from the BCG (see Fig. 1). As for RX J2129−GGL1, we note that the multiple images are being sheared in a direction almost perpendicular to the direction of the cluster centre. Based on the spectroscopic redshift for the lens and the source, $z_l = 0.3835$ and $z_s = 1.112$, respectively (Section 2.2.1), the lens is a foreground galaxy and not a cluster member.

Morphologically, the GGL system can be split into two different regions of similar colours whose positions are listed in Table B5

and shown in Fig. 8. Each of them produces four multiple images, with A.4 and B.4 being coincident. We constrain the GGL using images A.1–A.3 and B.1–B.4. The best-fitting model for this GGL is presented in Table B6.

3.3.1 Model I

For the lens, the core radius is neglected and fixed to 0, and the $r_{\rm cut}$ is arbitrarily set to a value of 50 kpc. The best-fitting model predicts the position of the multiple images with an rms of 0.20 arcsec (see Table 3). Fig. 8 shows the predicted positions of the multiple images with yellow diamonds. We see that the prediction reproduces the observed general shape of the system, but does not accurately recover the position of each multiple images.

3.3.2 Model II

Following the method described previously, we build a model that constrain the GGL lens parameters and the amplitude and orientation of a constant external shear at the redshift of the cluster. The addition of the shear brings more precision on the prediction of the multiple images as shown in Fig. 8 (red boxes) and in Table 3 with an rms of 0.07 arcsec. We note that the main arc and the counter-image in this system are unusually separated in the east–west direction, which is similar to the orientation of the shear as illustrated with the ellipse in the lower left-hand corner of Fig. 8. This ellipse shows that the shear seems to be oriented almost perpendicular to the cluster BCG direction.

3.3.3 Model III

For this model, the two cluster-scale components were modelled by two dPIEs with a cut radius $r_{\rm cut}$ of 1000 kpc. LENSTOOL optimizes all the other parameters of the profile. The first halo position is centred on the BCG and allowed to vary within a 5×5 arcsec^2 box. The second halo is allowed to move in a 30×50 arcsec^2 area around its input position (RA: 52.4131055; Dec.: −2.1914207). The BCG and the GGL lens are optimized as galaxy-scale dPIE potentials. Only their velocity dispersion is being optimized. The other parameters are fixed to the observed light distribution and typical values for galaxy and BCG potentials assuming they follow the scaling relation. The cluster members are being optimized following the Faber–Jackson scaling-relation (Faber & Jackson 1976) using the $F160W$ band as reference. The model is constrained by all the multiple images systems presented in Table B5. The best-fitting parameters are given in Table B6. The rms obtained is 0.10 arcsec compared to 0.07 arcsec for model II. The predicted multiple images are shown in Fig. 8 as cyan crosses. The overall shape of the system is well recovered even if system #A seems to be predicted with less precision than system #B.

The best-fitting model gives a redshift $z_{s3} = 2.58 \pm 0.05$ for system #3. This value is in good agreement with the one derived by Zitrin et al. (2015): $2.15 < z < 3.39$.

3.3.4 Model IV

The central galaxy of MACS J0329−GGL1 is not a cluster member. Thus, the GGL lens is not included in MACS J0329 cluster model IV. The resulting shear magnitude and orientation measurements are plotted in Fig. 9. Their values overlap with the ones from model III but are slightly more extended towards higher shear magnitude. Both of them remain within the 2σ contours of model II. Fig. 9 shows that this model of MACS J0329 tends to overestimate the amplitude of the shear at the location of the GGL. Also, the addition of the GGL in the model does not seem to constrain the shear at its particular location. The predicted redshift for system #3 is $z_{s3} = 2.59^{+0.06}_{-0.05}$, in good agreement with our previous results.

3.4 MACS J1149

We used the MACS J1149 ($z_c = 0.544$) model presented in Jauzac et al. (2016). This model combines five cluster-scale haloes (see Fig. 1) with 212 galaxy-scale haloes modelling cluster members. The model is constrained by 65 systems of multiple images.

MACS J1149−GGL1 is located north of the BCG at a distance of 137.9 arcsec (see Fig. 1 and Table 1). In Fig. 1, the right-hand panel shows the Einstein cross with its four images well separated from the lens. The lens galaxy has a measured spectroscopic redshift of $z_l = 0.542$, compatible with the cluster redshift. The source has a measured spectroscopic redshift of $z_s = 1.806$ (see Table 1).

The Jauzac et al. (2016) model did not include the lens as one of the cluster member; thus, we added it as a new galaxy potential. Since the lens does not have photometry in the $F814W$ band used in the scaling relations, we correct the measured $F775W$ magnitude to $F814W$ using the predicted colours for an elliptical galaxy at the cluster redshift (using the empirical template from Coleman et al. 1980) and use that value ($m_{F814W} = 20.11$) for the scaling relation.

3.4.1 Model I

The GGL is modelled here as a galaxy-scale dPIE. The only parameter optimized is the velocity dispersion of the central galaxy. The geometrical parameters are being fixed to the ones from the light distribution while $r_{\rm core}$ is set to 0 and $r_{\rm cut}$ to 50 kpc. The predicted positions of the multiple images are presented in Fig. 10. They are aligned with the axes of the light distribution of the lens, but not the observed ones. The rms is 0.26 arcsec (see Table. 3).

3.4.2 Model II

The environment is modelled by a constant external shear constrained by the multiple images of the GGL together with the central lens. The resulting rms is 0.07 arcsec. In Fig. 10, the predicted positions of the multiple images are shown by the red squares and are in good agreement with the observed ones. The ellipse in the bottom left-hand corner of the figure represents the external shear and its orientation (perpendicular to the direction of the main cluster halo and the BCG).

3.4.3 Model III

This model is based on the work by Jauzac et al. (2016) to which we add the potential of the GGL lens. The list of constraints is presented in Table B3. We include all the multiple image systems from the Jauzac et al. (2016) model, but only use the central bulge of system #1 as constraints and not all the star-forming regions of this spiral lensed galaxy.

The predicted positions of the multiple images can be seen on Fig. 10 as cyan crosses. The east and west images are well predicted, while the north and south images are predicted closer to the lens than observed. This may be due to a more important shear than the measured one as shown in Fig. 11. The shear intensity is predicted

higher in this model that in model II. There is still an improvement with respect to model I in predicting the multiple images positions, with an rms of 0.17 arcsec (Table 3).

Figs 10 and 11 show that the local shear magnitude of this model is overestimated by a factor of 2.5 compared to the external shear model prediction. However, its orientation is coherent with a difference smaller than 1°.2 compared to the best predicted one with the external shear.

3.4.4 Model IV

This model is the same as model III, without the multiple images of the GGL as constraints, and with the GGL lens optimized as a cluster member through the scaling relation. The measured shear is plotted in Fig. 11. It shows that the shear orientation is the same as the one measured in the two others models, but the shear magnitude is higher than the ones from models II and III.

4 DISCUSSION

4.1 GGL parameter degeneracy

In all our models, we fixed the value of the $r_{\rm cut}$ parameter in order to break its degeneracy with σ_0 according to Richard et al. (2010b). However, simple models optimizing both parameters were made to check the status of the degeneracy using only GGLs constraints. For the three GGLs, the multiple images did not provide enough information to constrain $r_{\rm cut}$. Yet, σ_0 is strongly degenerated for low $r_{\rm cut}$ values but manage to be constrained in those models due to its extremely low evolution with increasing $r_{\rm cut}$ over 25 kpc. This indicates that for the typical values chosen for fixing $r_{\rm cut}$, which are around 50 kpc, σ_0 is independent of this prior. Therefore, one can compare the results of optimizations of σ_0 without having to take in account the results on $r_{\rm cut}$.

4.2 Constraining the local shear with GGLs

For all three cases presented in this work, we find that including the detailed mass distribution of the cluster cores systematically improves the modelling of the GGL systems (Table 3). The rms of the multiple images decreases in all cases by at least a factor of 1.5 with respect to the results obtained from models assuming a single galaxy lens alone.

However, we note that the best rmss are always achieved for models that include an external shear instead of a detailed cluster mass distribution. External shear models provide a measurement of the magnitude and orientation of the local shear due to the environment of the GGL without any knowledge of its nature. Our results suggest that the cluster itself is not the only shear source. One can argue about the robustness of a model that simple, and therefore the precision of the constraints the GGL provides on the local shear. For example, the knowledge of the source redshift can add some systematic uncertainties on the shear measurements. We can also test the values obtained against independent measurements coming from weak-lensing.

4.2.1 Impact of source redshift

Among the three possible maxima of the photometric redshift probability distribution of the *Snail* (Section 2.2.2, Fig. 5), we have so far assumed the middle peak $z = 1.61$ for our models. Both the external shear and the velocity dispersion of the lens are degenerated with the source redshift; thus, none of them can directly constrain the redshift. We build a series of models with external shear for different fixed source redshifts between $z = 0.5$ and 2.5, letting σ_0, the shear magnitude, γ, and its orientation, θ, being optimized. The results of this test are presented in Fig. 12. Under the assumption that the lens of the *Snail* follows the general scaling relation of cluster members (Section 3.1), its velocity dispersion should be $\sigma_0 = 188\,{\rm km\,s^{-1}}$. This indicates that a source redshift $z = 1.6$ corresponds better to this assumption than $z = 1.1$ or 2.4.

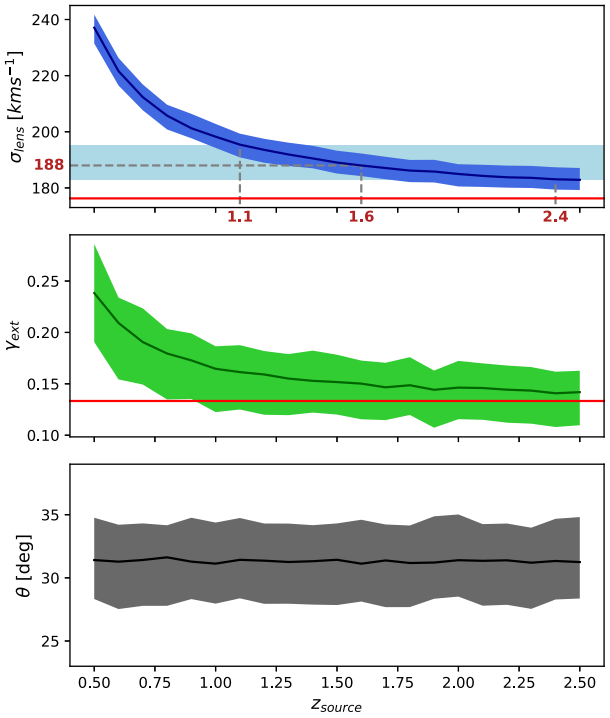

Figure 12. Velocity dispersion of the *Snail* lens, external shear amplitude, and orientation *versus* the redshift of the GGL source. The red lines show the values for $z_{\rm s} = 10$. In the upper panel, the grey lines show $z_{\rm s} = 1.1$, 1.6, 2.4, and $\sigma_0 = 188\,{\rm km\,s^{-1}}$, the light blue area shows the variation on σ_0.

Fig. 12 shows the evolution of the lens and the shear parameters as a function of the redshift. First, we note that the orientation of the shear is independent of the source redshift. Then, we observe that σ_0 and γ have a strong evolution for redshift $z < 1$. For redshift $z > 1$, the evolution is slower; thus, the variation in the values of σ_0 and γ due to redshift uncertainties is less important. For a source at redshift $z = 1.1$, the resulting velocity dispersion for the *Snail* lens would be $\sigma_0 = 195 \pm 5\,{\rm km\,s^{-1}}$. This result varies by 3.7 per cent compared to the one presented in Table B2. The variation of γ is 6.7 per cent from $\gamma = 0.15^{+0.04}_{-0.03}$ for $z_{\rm s} = 1.61$ to $\gamma = 0.16^{+0.04}_{-0.03}$ for $z_{\rm s} = 1.1$. The variation in the results of γ is smaller than the statistical errors from the models and the variation in results of σ_0 has the same order of magnitude as the statistical errors of the models. Therefore, a photometric redshift seems precise enough to derive the properties of the lens and its environment in the case of a simple model.

4.2.2 Comparison with weak-lensing constraints

Weak-lensing is the usual measurement to be used to estimate the shear produced by the direct environment. By measuring the shape

of the background sources as observed in the cluster, we obtain an independent estimation of the shear signal at large radii from the core (i.e. outside the strong-lensing region).

Following the methodology described in Jauzac et al. (2012, 2015), we construct the background galaxy catalogues using the *HST* data. We give only a brief description and refer the reader to the former papers for more details. The detection of sources is done using SEXTRACTOR (Bertin & Arnouts 1996) in the $F814W$ band, and the galaxy shapes are measured using the RRG method (Rhodes, Refregier & Groth 2000). RRG was developed for measurements on *HST*/ACS observations and therefore includes corrections of the point spread function (PSF). One of the careful steps in the build-up of the weak-lensing catalogue is the removal of the foreground and cluster galaxies that would otherwise dilute the shear signal. To counteract this problem, as we do not have a redshift for all sources, we identify the regions populated by these different galaxy populations in the colour–colour space mag_{F435W}–mag_{F606W}–mag_{F814W}, and exclude them from our final catalogue. This colour–colour selection is calibrated using the publicly available photometric redshifts from the CLASH collaboration (Postman et al. 2012). We further apply standard lensing cuts: (1) on the size of the galaxies to remove galaxies with a size close to the one of the PSF (>0.13 arcsec); and (2) on the detection limit of the sources with a signal-to-noise ratio greater than 4.5. Our final catalogue contains 385 galaxies, resulting in a density of background sources of ∼50 galaxies arcmin^{-2}.

From this weak-lensing catalogue, we can then measure both the tangential and radial shear profiles for RX J2129, γ_t and γ_x, respectively, using the following inversion relations:

$$\gamma_t = -(\gamma_1 \times \cos(2\alpha) + \gamma_2 \times \sin(2\alpha)) \quad (4)$$

and

$$\gamma_x = -\gamma_1 \times \sin(2\alpha) + \gamma_2 \times \cos(2\alpha), \quad (5)$$

where γ_1 and γ_2 are provided by RRG and α is the position angle between the vector pointing in the decreasing RA direction (west) and the vector connecting the BCG to the background source. As the redshift of all weak-lensing galaxies is not known, we need to assume a background redshift distribution. For this purpose, we make use of the HFF Abell 2744 photometric redshift catalogue provided as part of the HFF–DeepSpace project (Shipley et al. 2018). We only consider the distribution of sources at a redshift higher than the clusters RX J2129 and Abell 2744, i.e. $z > 0.4$, and with a photometric redshift error better than 10 per cent. We further apply a magnitude cut, $m_{F814W} < 25.5$, in order to match the depth of the RX J2129 images. Random redshifts are drawn from this distribution and assigned to our catalogue sources. The average γ_t and γ_x are then calculated in annuli of 20 arcsec centred on the BCG. This process is repeated 100 times, and the final values considered here are the means and their respective standard deviations of these 100 realizations.

Fig. 13 shows the comparison of the tangential (γ_t) and radial (γ_x) shear profiles as a function of the radius from the BCG obtained with different measurement methods: the weak-lensing analysis from high-resolution *HST* images (blue filled circles), and the predicted external shear from the strong-lensing model of the cluster core (green filled circles). These profiles are also compared to the shear profile measured by Okabe et al. (2010, black filled circles) and their single isothermal sphere (SIS) fit (black line). The external shear value from model II is highlighted by the red star.

At the location of the *Snail* (a region comprised within 60 and 120 arcsec from the cluster BCG), we observe an excellent agreement between the weak-lensing shear measured in this paper, the strong-lensing extrapolation, the measurements from Okabe et al. (2010), and the predicted shear value from the external shear model (model II).

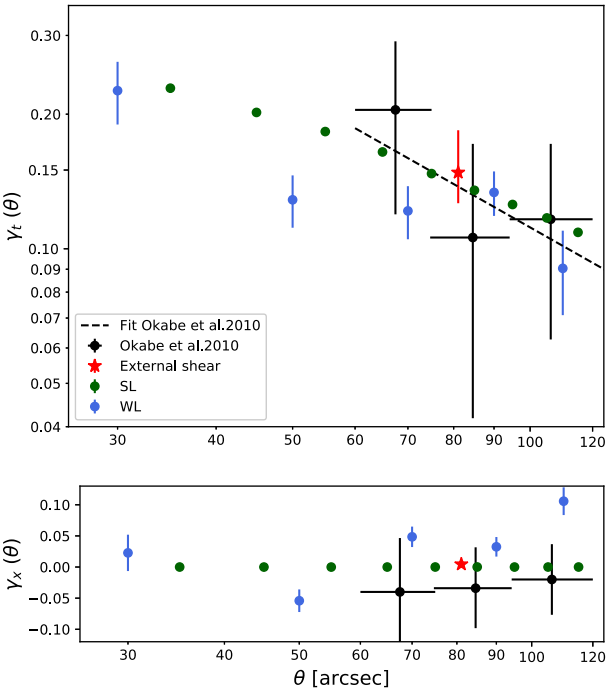

Figure 13. Shear component profile (tangential γ_t and radial γ_x) as a function of radius from BCG. In blue, the shear derived from the CLASH data weak-lensing analysis. In green, the shear predicted by the RX J2129 complete cluster model. In black, the shear measurement and the predicted shear with the SIS model from Okabe et al. (2010). The shear estimated with the external shear model is represented with the red star.

Both direct weak-lensing measurements show a really good agreement. The ground-based values from Okabe et al. (2010) have larger error bars due to the lower background galaxy density, ∼30 galaxies arcmin^{-2}, compared to our *HST* measurement.

We further compare our *HST* weak-lensing measurement with the predicted external shear of model II. One can see that the predicted external shear is similar to the *HST* weak-lensing shear, including its error estimate. This agreement reveals the potential for GGL to locally probe the shear profile in the outskirts of clusters. The annulus around the GGL radius encompasses ∼100 weak-lensing background galaxies ($80 < R < 100$ arcsec) and thus have a local source density of ∼35 galaxies arcmin^{-2}. That means a single GGL event in an area of ∼9 arcsec^2 provides a shear measurement equivalent to a standard *HST* weak-lensing analysis over an area of ∼3 arcmin^2. However, this is only true when the studied cluster is being relaxed, i.e. no substructures in its outskirts. In our sample of GGLs, only RX J2129−GGL1 is observed in a relatively relaxed cluster. This is why we used it to show the strength of GGL local shear measurements.

4.3 Simple constraints on the cluster based on external shear

Tu et al. (2008) showed that some partial information about the cluster mass distribution can be retrieved purely based on GGL analysis, as they derive the position of the centre of Abell 1689 cluster with three GGLs. Here, we test whether we can blindly retrieve the directions of the clusters from the GGLs positions and

estimates of their central velocity dispersion from the external shear models, under the assumption that this shear is dominated by the presence of the cluster.

We can give the direction of the centre of the cluster for RX J2129 using the orientation of the shear that is supposed to be perpendicular to the direction towards the cluster. The values computed for all the cluster in our study are in Table 4. The measured angle from the GGL to the BCG is $-57.^{\circ}0 \pm 0.^{\circ}4$, and the angle given by the external shear is $-58.^{\circ}5^{+3.^{\circ}3}_{-3.^{\circ}2}$. We have a good agreement on this value.

Assuming that the cluster modelled by an SIS, we can also compute the velocity dispersion of the cluster from the shear magnitude γ (Dye et al. 2007). The relation between σ_0 and γ is

$$\sigma_0 = \sqrt{\frac{\gamma c^2 R}{2\pi D_{\rm LS}/D_{\rm OS}}},$$

where R is the distance between the GGL and the cluster and $D_{\rm LS}/D_{\rm OS}$ is the ratio of the angular diameter distances between the lens and the source, and between the observer and the source. In the case of RX J2129, we obtain $\sigma_{\rm RXJ2129} = 912^{+105}_{-70}\,{\rm km\,s^{-1}}$. This result is matching the results of the one of the complete cluster model (see Table B2) even if we only assume here the contribution of the cluster clump of DM. We can note also that our result is also in agreement with the $\sigma_{\rm SIS}$ of Okabe et al. (2010).

As seen in Section 4.2.1, for RX J2129, the photometric redshift of the *Snail* source increases our uncertainty on the external shear. The result of the process using the shear compatible with a source at $z_{\rm s} = 1.1$ is $\sigma = 952^{+102}_{-81}\,{\rm km\,s^{-1}}$, thus a 4.3 per cent variation to the previous result. This value is still consistent with the complete model of the cluster within error bars, and once again the variation is less significant than the error on the value. Finally, for RX J2129, as seen in Fig. 12, the result for the direction of the cluster remains unchanged with the change of redshift.

The same procedure was applied for the two other clusters and all the results can be found in Table 4. We can see that the predicted orientation of the shear is a good indicator of the position of the cluster centre. Comparing the velocity dispersions of the SIS to the ones predicted by model III (see Tables B2, B4, and B6), we note that the only cluster with a good agreement is RX J2129. This can be explained by the simplicity of the cluster structure, only one cluster halo of DM, and thus the absence of substructures in its surroundings. Also, we only assumed here the contribution of the cluster but not the one from the BCG and the cluster members. That could explain the systematic higher value of σ_0 for all of the three clusters. In any case, this method provides a blind estimate of the cluster velocity dispersion without the need for constraints by multiple images near its core.

4.4 Combining GGLs with cluster core models

The strong-lensing constraints of the GGLs allow to measure locally the influence of the cluster at large radii. But this influence is only a second-order effect, as the clusters enhance the lensing power of the single galaxies and produce a shear. Figs 7, 9, and 11 show that the GGLs constraints only have a small influence on the cluster core models. We can see that the contours of the complete models of the clusters tend to get closer to the results of the external shear models when the GGLs constraints are taken in account, but the shear is not perfectly reproduced, leading to a higher rms in the prediction of the multiple images than models with external shear (see Table 3). This lack of influence can be the fact of the GGLs constraints being only one more system of multiple images among others that are closer to the core, thus having more influence. The clusters parametric models might be too constrained by those multiple images in the cores to reproduce correctly both the core and the outskirts structures. New parameters bringing new degrees of freedom, especially in the outskirts, could be a solution as long as they do not lead to an overfit of the model. One other explanation of the difference between external shear models and complete cluster models results would be that the influence of the cluster is only a part of the environment shear. Fig. 1 shows that for MACS 0329 and MACS 1149, the GGLs are at the edge of the ACS data. The environment influence might not be completely accounted for, thus explaining the small difference made by the addition of the GGLs constraints in Figs 9 and 11. For RX J2129, the GGLs is closer to the BCG than in the other two cases; thus, its environment is better known and the shear prediction of the cluster model (Fig. 7) seems more affected by the GGL constraints, supporting this solution.

For GGLs for which the lens is part of the cluster, the multiple images directly constrain the massive cluster members. If the spectroscopic redshift of the source is known, we can determine if the galaxy lies on top of the scaling relation or not by having an independent measurement of its parameters. For MACS 1149−GGL1, we know the redshift and thus we can compare the values of the model with the expected scaling relations described in Section 3.1 using $\sigma_0^* = 158\,{\rm km\,s^{-1}}$ from Bernardi et al. (2003). The expected value is $\sigma_0 = 178^{+31}_{-30}\,{\rm km\,s^{-1}}$, which is in agreement with the model values in Table B4, mostly the one of the most complete cluster model. The two other results are closer to the upper limit value because those models do not take in account the impact of the cluster convergence boosting the lensing power of the galaxy, therefore leading to an overestimation of the velocity dispersion of the lens. However the value of σ_0^* of the complete cluster model is ∼40 per cent higher than the one optimized in the cluster model. This could indicate that the standard galaxy is not constrained well enough, as the cluster model not including the GGL constraints provides different values. We find a similar problem in the cluster model of RX J2129 where $\sigma_0^* = 93 \pm 16\,{\rm km\,s^{-1}}$. If the GGL lens follows the scaling relation as we assumed it, the velocity dispersion of the lens would be $\sigma = 114\,{\rm km\,s^{-1}}$, which is far too low according to Fig. 12 to produce multiple images as we observe them even for a source with $z_{\rm s} = 10$. Even with the boost of the cluster, a complete model constraining the GGL parameters with a source with $z_{\rm s} = 10$ leads to a $\sigma_0 = 166.8\ {\rm km\,s^{-1}}$. There is a ∼30 per cent variation with this value and the one derived from the scaled standard galaxies in the models presented in Table B2. Either the standard galaxy parameters are not well constrained or our assumption about the GGL lens is wrong. Having a spectroscopic redshift for the GGL source would provide a way to constrain σ_0 independently of the scaling relation and would allow us to test the consistency of the results. Then, assuming that the galaxy follows this relation, we could constrain better the standard galaxy parameters directly using the locations of multiple images in the GGLs. For this reason, a spectroscopic follow-up of the 24 GGLs presented in Fig. A1 and Table A1 would improve greatly the model constraints for all those clusters.

5 SUMMARY AND CONCLUSIONS

We visually inspect the full *Hubble* field of view of the 25 observed clusters from the CLASH survey in order to locate GGL events in the outskirts of those clusters. We find a selection of 24 candidate GGLs (some already known), and study in detail three of them presenting the following characteristics: a single lens, at least four distinct multiple images, and a separation from the BCG larger than

80 arcsec. For each of those GGLs and their associated cluster, we produce four parametric models of the DM distribution to study the influence of the cluster on the GGL modelling and the influence on the GGL on the cluster models.

Through those models, we show that the modelling of the GGLs cannot be done properly without taking into account its environment. This can be achieved through a complete model of the neighbour structures or even with a simple parametrization of their effects like an external shear.

A photometric redshift is accurate enough to properly estimate the strength of the shear as the uncertainties bring a variation that is smaller to the statistical errors on the measurement. The orientation of the shear is always well estimated as it is redshift-independent. The measurement of the local external shear has a similar quality as independent measurements of the shear through weak-lensing.

The constrained local shear magnitude and orientation are precise enough to properly derive the direction towards the cluster core, and its central velocity dispersion assuming an SIS distribution of the DM halo when the cluster structure is simple. For more complex clusters, the velocity dispersion of the central clump is overestimated. Therefore, the strong-lensing constraints of the GGLs allow an independent estimate or provide an upper limit to the properties of a neighbour cluster without the need of multiple images in the core to constrain it.

When combined with a complete cluster strong-lensing model, the first-order effect of the GGL constraints is to constrain with precision the DM halo of the lens galaxy. However, they bring only a little information to the parameters of the core as its influence is a second-order effect. Therefore, the complete cluster models do not reproduce the GGLs multiple images as well as the external shear models do. This can be the sign of the parametric models not having enough freedom in the outskirts to constrain the DM distribution or that our knowledge of the environment is not complete enough as the GGLs lie at the edge of the ACS fields.

In the case of GGL lenses that are also cluster members, there are inconsistencies between the derived scaling relations and the GGL lens properties. The knowledge of the spectroscopic redshifts of the sources could allow to study the link between the massive cluster members in the outskirts and the scaling relation.

A spectroscopic follow-up of the GGLs presented in this work would confirm their nature as GGLs, and bring independent estimates on the cluster mass profiles at large radii. For lenses located in the cluster, it could also bring constraints on the scaling relations assumed in galaxy cluster models.

ACKNOWLEDGEMENTS

GD, JR, JM, and BC acknowledge support from the European Research Council starting grant 336736-CALENDS. GD also acknowledges a grant from the Swiss National Science Foundation. MJ was supported by the Science and Technology Facilities Council [grant numbers ST/L00075X/1 and ST/P000541/1]. We acknowledge fruitful discussions with Jean-Paul Kneib, Eric Jullo, and Marceau Limousin. Based on observations made with ESO Telescopes at the La Silla Paranal Observatory under programme ID 186.A-0798. Based on observations obtained with the NASA/ESA *Hubble Space Telescope*, retrieved from the Mikulski Archive for Space Telescopes (MAST) at the Space Telescope Science Institute (STScI). STScI is operated by the Association of Universities for Research in Astronomy, Inc. under NASA contract NAS 5-26555. Also based on data obtained at the W.M. Keck Observatory, which is operated as a scientific partnership among the California Institute of Technology, the University of California, and the National Aeronautics and Space Administration. The Observatory was made possible by the generous financial support of the W.M. Keck Foundation. The authors wish to recognize and acknowledge the very significant cultural role and reverence that the summit of Mauna Kea has always had within the indigenous Hawaiian community. We are most fortunate to have the opportunity to conduct observations from this mountain. This work is based on data and catalogue products from HFF–DeepSpace, funded by the National Science Foundation and Space Telescope Science Institute (operated by the Association of Universities for Research in Astronomy, Inc., under NASA contract NAS5-26555).

REFERENCES

Barden M., Häußler B., Peng C. Y., McIntosh D. H., Guo Y., 2012, MNRAS, 422, 449
Bartelmann M., Schneider P., 2001, Phys. Rep., 340, 291
Belli S., Jones T., Ellis R. S., Richard J., 2013, ApJ, 772, 141
Bernardi M. et al., 2003, AJ, 125, 1849
Bertin E., Arnouts S., 1996, A&AS, 117, 393
Bolzonella M., Miralles J.-M., Pelló R., 2011, Astrophysics Source Code Library, ascl:1108.010
Bradač M. et al., 2008, ApJ, 681, 187
Bradač M., Schneider P., Lombardi M., Erben T., 2005, A&A, 437, 39
Bruzual G., Charlot S., 2003, MNRAS, 344, 1000
Calzetti D., Armus L., Bohlin R. C., Kinney A. L., Koornneef J., Storchi-Bergmann T., 2000, ApJ, 533, 682
Coleman D., Wu C., Weedman D., 1980, ApJS, 43, 393
Diego J. M., Broadhurst T., Benitez N., Lim J., Lam D., 2015, MNRAS, 449, 588
Dye S., Smail I., Swinbank A. M., Ebeling H., Edge A. C., 2007, MNRAS, 379, 308
Ebeling H., Ma C. J., Kneib J.-P., Jullo E., Courtney N. J. D., Barrett E., Edge A. C., Le Borgne J.-F., 2009, MNRAS, 395, 1213
Elíasdóttir Á. et al., 2007, preprint (arXiv:0710.5636)
Faber S. M., Jackson R. E., 1976, ApJ, 204, 668
Faure C. et al., 2008, ApJS, 176, 19
Grillo C. et al., 2015, ApJ, 800, 38
Hoekstra H., Bartelmann M., Dahle H., Israel H., Limousin M., Meneghetti M., 2013, Space Sci. Rev., 177, 75
Jauzac M. et al., 2012, MNRAS, 426, 3369
Jauzac M. et al., 2015, MNRAS, 446, 4132
Jauzac M. et al., 2016, MNRAS, 457, 2029
Jauzac M. et al., 2017, preprint (arXiv:1711.01324)
Jullo E., Kneib J.-P., Limousin M., Elíasdóttir Á., Marshall P. J., Verdugo T., 2007, New J. Phys., 9, 447
Kneib J.-P., 1993, PhD thesis, Université Paul Sabatier, Toulouse
Kneib J.-P., Natarajan P., 2011, A&AR, 19, 47
Le Fèvre O. et al., 2003, in Iye M., Moorwood A. F. M., eds, Proc. SPIE Conf. Ser. Vol. 4841, Instrument Design and Performance for Optical/Infrared Ground-based Telescopes. SPIE, Bellingham, p. 1670
Limousin M. et al., 2007, ApJ, 668, 643
Limousin M. et al., 2010, A&A, 524, A95
Lin Y.-T., Mohr J. J., Gonzalez A. H., Stanford S. A., 2006, ApJ, 650, L99
Lotz J. M. et al., 2017, ApJ, 837, 97
Massey R., Kitching T., Richard J., 2010, Rep. Prog. Phys., 73, 086901
Medezinski E. et al., 2013, ApJ, 777, 43
Merten J. et al., 2011, MNRAS, 417, 333
Okabe N., Takada M., Umetsu K., Futamase T., Smith G. P., 2010, PASJ, 62, 811
Oke J. B. et al., 1995, PASP, 107, 375
Peng C. Y., , Ho L. C., Impey C. D., Rix H.-W., 2011, Astrophysics Source Code Library, ascl:1104.010
Postman M. et al., 2012, Astrophys. J. Suppl. Ser., 199, 25
Rhodes J., Refregier A., Groth E. J., 2000, ApJ, 536, 79

Richard J. et al., 2010b, MNRAS, 404, 325
Richard J. et al., 2014, MNRAS, 444, 268
Richard J., Kneib J.-P., Limousin M., Edge A., Jullo E., 2010a, MNRAS, 402, L44
Richard J., Kneib J.-P., Ebeling H., Stark D. P., Egami E., Fiedler A. K., 2011, MNRAS, 414, L31
Rosati P. et al., 2014, The Messenger, 158, 48
Salpeter E. E., 1955, ApJ, 121, 161
Schechter P. L. et al., 1997, ApJ, 475, L85
Scott D., 1992, Multivariate Density Estimation : Theory, Practice and Visualization. Wiley, New York, NY
Seidel G., Bartelmann M., 2007, A&A, 472, 341
Shipley H. V. et al., 2018, ApJS, 235, 14
Smith G. P. et al., 2009, ApJ, 707, L163
Smith G. P., Kneib J.-P., Smail I., Mazzotta P., Ebeling H., Czoske O., 2005, MNRAS, 359, 417
Sonnenfeld A. et al., 2017, Publ. Astron. Soc. Japan, 70, S29
Soucail G., Mellier Y., Fort B., Mathez G., Cailloux M., 1988, A&A, 191, L19
Steidel C. C., Shapley A. E., Pettini M., Adelberger K. L., Erb D. K., Reddy N. A., Hunt M. P., 2004, ApJ, 604, 534
Tu H., Limousin M., Fort B., Shu C. G., Sygnet J. F., Jullo E., Kneib J. P., Richard J., 2008, MNRAS, 386, 1169
Umetsu K. et al., 2015, ApJ, 806, 207
Vanzella E. et al., 2017, ApJ, 842, 47
Wagner J., Bartelmann M., 2016, A&A, 590, A34
Wong K. C., Ishida T., Tamura Y., Suyu S. H., Oguri M., Matsushita S., 2017, ApJ, 843, L35
Zitrin A. et al., 2012, ApJ, 747, L9
Zitrin A. et al., 2015, ApJ, 801, 44
Zitrin A., Broadhurst T., Barkana R., Rephaeli Y., Benítez N., 2011, MNRAS, 410, 1939

APPENDIX A: GALAXY–GALAXY LENSING IN CLASH

We list here for reference all the GGL systems we have found from visual inspection of all the CLASH *HST* images.

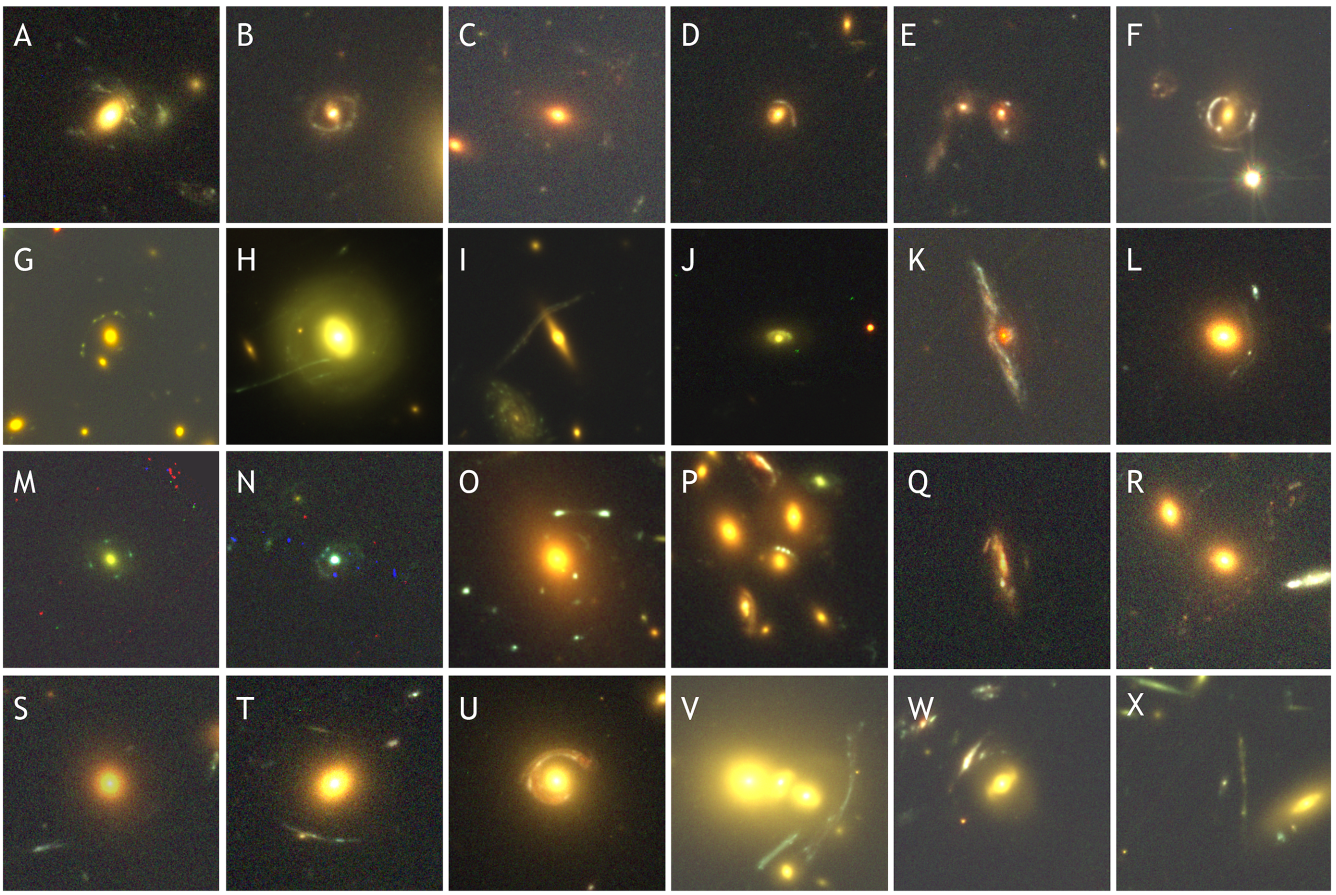

Figure A1. GGLs found in the CLASH images. All the pictures are 10 arcsec across. J, B(*F435W+F475W*), G (*F555W+F606W*), and R (*F775W+F814W+F850LP*). G, H, I, J, O, P, V, W, and X image frontier fields: R(*F814W*), G(*F606W*), and B(*F435W*).

Table A1. Catalogue of the GGL found in the CLASH data. When relevant, we provide the name used in previous works mentioning the same systems.

ID	Image	α	δ	Previous reference
A209−GGL1	A	22.9577568	−13.6032558	
A209−GGL2	B	22.9648793	−13.6363138	
A383−GGL1	C	42.0113589	−3.5480288	
MACS0429−GGL1	D	67.4020771	−2.8713932	
MACS0429−GGL2	E	67.3892478	−2.8741192	
MACS0329−GGL1*	F	52.4201304	−2.2216321	
MACS0416−GGL1	G	64.0340808	−24.0667448	ID14 from Vanzella et al. (2017)
MACS0416−GGL2	H	64.0284705	−24.085668	
MACS0416−GGL3	I	64.0170899	−24.0895541	'Dragon Kick' from Diego et al. (2015)
MACS0717−GGL1	J	109.3786176	37.77722736	
MACS0744−GGL1	K	116.2121685	39.4598681	
MACS1115−GGL1	L	168.9562589	1.4974098	
MACS1149−GGL1*	M	177.4028221	22.4366292	
MACS1149−GGL2	N	177.4116004	22.4296659	
MACS1149−GGL3	O	177.403888	22.4266297	A6 system from Smith et al. (2009)
MACS1149−GGL4	P	177.3931348	22.4113364	A5 system from Smith et al. (2009)
RX J1347−GGL1	Q	206.8960322	−11.7536032	
RXJ1347−GGL2	R	206.865999	−11.7649203	F system from Bradač et al. (2008)
RX J1347−GGL3	S	206.8725903	−11.7673974	G system from Bradač et al. (2008)
MS2137−GGL1	T	325.0615233	−23.6511738	
RX J2129−GGL1*	U	322.4287798	0.1080707	
SMACS2248−GGL1	V	342.2156577	−44.5183953	
SMACS2248−GGL2	W	342.1557424	−44.5459123	
SMACS2248−GGL3	X	342.1633643	−44.5297236	

*GGLs studied in this work.

APPENDIX B: MULTIPLE IMAGES SYSTEMS IN THE CLUSTERS

Table B1. Multiple images used in the RX J2129 models. The results on the redshifts estimation are the ones of model III.

ID	α (°)	δ (°)	$z_{\rm prior}$	$z_{\rm model}$
A.1	21:29:42.85	00:06:30.27	1.61	
A.2	21:29:42.96	00:06:29.99	1.61	
A.3	21:29:42.99	00:06:29.06	1.61	
A.4	21:29:42.88	00:06:28.45	1.61	
1.1	21:29:40.89	00:05:17.95	1.522	
1.2	21:29:40.84	00:05:23.15	1.522	
1.3	21:29:40.31	00:05:35.76	1.522	
3.1	21:29:40.44	00:05:07.68	[0.2–2.0]	$1.49^{+0.17}_{-0.09}$
3.2	21:29:40.24	00:05:24.97		
3.3	21:29:39.77	00:05:31.99		
5.1	21:29:39.98	00:05:15.87	[0.2–2.0]	$0.78^{+0.05}_{-0.03}$
5.2	21:29:39.90	00:05:17.17		

Table B2. Parameters for the RX J2129 models.

Potential	$\Delta\alpha$ (arcsec)	$\Delta\delta$ (arcsec)	e	θ (°)	$r_{\rm core}$ (kpc)	$r_{\rm cut}$ (kpc)	σ_0 (km s^{-1})	γ
Model I								
GGL	[− 44.2]	[68.0]	[0.11]	[− 50.6]	[0]	[64]	222^{+1}_{-1}	
Model II								
GGL	[− 44.2]	[68.0]	[0.11]	[− 50.6]	[0]	[64]	188^{+4}_{-3}	
Ext Shear				$31.5^{+3.3}_{-3.2}$				$0.15^{+0.04}_{-0.03}$
Model III								
GGL	[− 44.2]	[68.0]	[0.11]	[− 50.6]	[0]	[64]	179^{+3}_{-4}	
DM1	$1.2^{+1.4}_{-1.2}$	$-1.0^{+0.8}_{-0.4}$	$0.59^{+0.05}_{-0.06}$	$-21.8^{+0.3}_{-0.4}$	49^{+8}_{-6}	[1000]	852^{+49}_{-27}	
BCG	[0.0]	[0.0]	[0.49]	[− 35.4]	[0]	[90]	220^{+17}_{-20}	
L* galaxy					[0.15]	[45]	93^{+16}_{-16}	
Model IV								
DM1	$0.9^{+1.3}_{-1.1}$	$-0.8^{+0.5}_{-0.6}$	$0.61^{+0.05}_{-0.07}$	$-21.6^{+0.4}_{-0.4}$	44^{+5}_{-4}	[1000]	824^{+25}_{-27}	
BCG	[0.0]	[0.0]	[0.49]	[− 35.4]	[0]	[90]	222^{+23}_{-19}	
L* galaxy					[0.15]	[45]	96^{+22}_{-22}	

Table B3. Multiple images used in the MACS1149 models. The results on the redshifts estimation are the ones of model III.

ID	α (°)	δ (°)	$z_{\rm prior}$	$z_{\rm model}$
A.1	11:49:36.61	22:26:12.08	1.806	
A.2	11:49:36.69	22:26:12.70	1.806	
A.3	11:49:36.74	22:26:11.59	1.806	
A.4	11:49:36.66	22:26:11.08	1.806	
1.1	11:49:35.28	22:23:45.63	1.4888	
1.2	11:49:35.86	22:23:50.78	1.4888	
1.3	11:49:36.82	22:24:08.73	1.4888	
2.1	11:49:36.58	22:23:23.06	1.894	
2.2	11:49:37.46	22:23:32.94	1.894	
2.3	11:49:37.58	22:23:34.37	1.894	
3.1	11:49:33.78	22:23:59.42	3.128	
3.2	11:49:34.25	22:24:11.07	3.128	
3.3	11:49:36.31	22:24:25.86	3.128	
4.1	11:49:34.32	22:23:48.57	2.95	
4.2	11:49:34.66	22:24:02.62	2.95	
4.3	11:49:37.01	22:24:22.03	2.95	
5.1	11:49:35.94	22:23:35.02	2.79	
5.2	11:49:36.27	22:23:37.77	2.79	
5.3	11:49:37.91	22:24:12.74	2.79	
6.1	11:49:35.93	22:23:33.16	[2.0–3.0]	$2.72^{+0.08}_{-0.06}$
6.2	11:49:36.43	22:23:37.89		
6.3	11:49:37.93	22:24:09.02		
7.1	11:49:35.75	22:23:28.80	[2.0–3.0]	$2.63^{+0.09}_{-0.06}$
7.2	11:49:36.81	22:23:39.37		
7.3	11:49:37.82	22:24:04.47		
8.1	11:49:35.64	22:23:39.66	[2.0–3.0]	$2.97^{+0.03}_{-0.03}$
8.2	11:49:35.95	22:23:42.20		
8.3	11:49:37.70	22:24:16.99		
9.1	11:49:37.24	22:25:34.40	0.981	
9.2	11:49:36.93	22:25:37.98	0.981	
9.3	11:49:36.78	22:25:38.00	0.981	
9.4	11:49:36.88	22:25:35.07	0.981	
10.1	11:49:37.07	22:25:31.83	[1.0–1.5]	$1.31^{+0.09}_{-0.06}$
10.2	11:49:36.87	22:25:32.26		
10.3	11:49:36.53	22:25:35.80		
13.1	11:49:36.89	22:23:52.03	[1.0–1.5]	$1.28^{+0.02}_{-0.01}$
13.2	11:49:36.68	22:23:47.96		
13.3	11:49:36.01	22:23:37.89		
14.1	11:49:34.00	22:24:12.61	[2.5–4.0]	$2.55^{+1.07}_{-0.06}$
14.2	11:49:33.80	22:24:09.45		
15.1	11:49:38.21	22:23:15.70	[2.0–8.0]	$3.38^{+0.15}_{-0.14}$
15.2	11:49:38.48	22:23:19.48		
15.3	11:49:37.50	22:23:07.26		
16.1	11:49:38.33	22:23:15.58	[1.0–6.0]	$4.83^{+1.94}_{-1.44}$
16.2	11:49:38.37	22:23:16.18		
17.1	11:49:38.39	22:23:14.04	[1.0–7.0]	$4.23^{+0.33}_{-0.29}$
17.2	11:49:38.70	22:23:18.45		
17.3	11:49:37.58	22:23:04.14		
18.1	11:49:38.30	22:23:11.98	[1.0–8.0]	$5.04^{+0.64}_{-0.56}$
18.2	11:49:38.90	22:23:20.61		
18.3	11:49:37.61	22:23:03.55		
21.1	11:49:34.28	22:24:46.33	[2.0–3.0]	$2.57^{+0.06}_{-0.07}$
21.2	11:49:34.45	22:24:47.10		
21.3	11:49:34.81	22:24:45.67		
22.1	11:49:36.96	22:23:34.44	3.216	
22.2	11:49:38.17	22:24:00.84	3.216	
22.3	11:49:36.04	22:23:24.54	3.216	
		...		

Table B3. *– continued.*

ID	α (°)	δ (°)	$z_{\rm prior}$	$z_{\rm model}$
		...		
26.1	11:49:37.14	22:25:33.52	[0.6–1.5]	$0.97^{+0.07}_{-0.07}$
26.2	11:49:36.87	22:25:33.88		
26.3	11:49:36.66	22:25:36.97		
29.1	11:49:37.92	22:23:20.60	[2.0–4.0]	$2.74^{+0.08}_{-0.15}$
29.2	11:49:38.18	22:23:25.46		
29.3	11:49:37.08	22:23:12.13		
31.1	11:49:36.52	22:23:48.29	[2.0–3.0]	$2.66^{+0.11}_{-0.05}$
31.2	11:49:34.87	22:23:30.60		
31.3	11:49:37.35	22:24:08.78		
34.1	11:49:37.97	22:23:17.22	[2.0–5.0]	$3.41^{+0.19}_{-0.15}$
34.2	11:49:38.49	22:23:26.24		
34.3	11:49:37.24	22:23:09.71		

Table B4. Table of the parameters of the models of MACS1149.

Potential	$\Delta\alpha$ (arcsec)	$\Delta\delta$ (arcsec)	e	θ (°)	$r_{\rm core}$ (kpc)	$r_{\rm cut}$ (kpc)	σ_0 (km s^{-1})	γ
Model I								
GGL	[− 13.6]	[137.2]	[0.17]	[120.0]	[0]	[50]	190^{+5}_{-2}	
Model II								
GGL	[− 13.6]	[137.2]	[0.17]	[120.0]	[0]	[50]	193^{+5}_{-5}	
Ext Shear				$7.2^{+10.4}_{-5.0}$				$0.13^{+0.08}_{-0.06}$
Model III								
GGL	[− 13.6]	[137.2]	[0.17]	[120.0]	[0]	[50]	174^{+28}_{-2}	
DM1	$-3.2^{+0.3}_{-0.3}$	$1.4^{+0.2}_{-0.2}$	$0.56^{+0.01}_{-0.01}$	$40.0^{+0.5}_{-0.3}$	92^{+2}_{-3}	[1000]	1015^{+5}_{-11}	
DM2	$-23.7^{+0.9}_{-0.5}$	$-28.0^{+1.0}_{-1.2}$	$0.17^{+0.06}_{-0.04}$	$128.6^{+6.2}_{-7.8}$	163^{+15}_{-25}	[1000]	124^{+32}_{-34}	
DM3	$-43.0^{+0.4}_{-1.0}$	$-53.0^{+0.4}_{-0.4}$	$0.64^{+0.08}_{-0.03}$	$30.1^{+3.8}_{-6.4}$	44^{+15}_{-15}	[1000]	403^{+27}_{-26}	
DM4	$18.9^{+0.5}_{-0.3}$	$47.2^{+1.5}_{-0.7}$	$0.65^{+0.09}_{-0.05}$	$124.9^{+8.4}_{-9.2}$	142^{+9}_{-9}	[1000]	482^{+40}_{-21}	
DM5	$-17.4^{+0.4}_{-0.4}$	$101.0^{+0.3}_{-0.3}$	$0.53^{+0.08}_{-0.03}$	$129.5^{+5.1}_{-9.4}$	9^{+4}_{-1}	[1000]	354^{+29}_{-11}	
BCG	[0.0]	[0.0]	[0.20]	[34.0]	36^{+3}_{-3}	118^{+21}_{-23}	256^{+21}_{-24}	
GAL1	[3.2]	[− 11.1]	$0.56^{+0.03}_{-0.03}$	$45.9^{+10.9}_{-6.3}$	[0]	68^{+2}_{-1}	208^{+10}_{-9}	
L* galaxy					[0.15]	44^{+3}_{-3}	198^{+2}_{-2}	
Model IV								
DM1	$-4.1^{+0.1}_{-0.6}$	$1.3^{+0.1}_{-1.1}$	$0.60^{+0.02}_{-0.01}$	$28.8^{+0.6}_{-6.6}$	99^{+2}_{-20}	[1000]	899^{+7}_{-62}	
DM2	$-25.3^{+0.2}_{-0.2}$	$-32.8^{+0.8}_{-0.3}$	$0.70^{+0.12}_{-0.01}$	$49.6^{+0.8}_{-8.9}$	66^{+7}_{-33}	[1000]	442^{+12}_{-16}	
DM3	$-48.3^{+0.6}_{-3.7}$	$-49.6^{+0.3}_{-1.1}$	$0.39^{+0.02}_{-0.04}$	$175.8^{+6.6}_{-36.3}$	221^{+10}_{-7}	[1000]	481^{+41}_{-11}	
DM4	$23.3^{+0.1}_{-1.1}$	$47.2^{+1.3}_{-0.2}$	$0.26^{+0.01}_{-0.11}$	$103.1^{+2.3}_{-10.9}$	76^{+2}_{-23}	[1000]	584^{+31}_{-11}	
DM5	$-16.3^{+0.1}_{-0.2}$	$100.3^{+0.0}_{-0.0}$	$0.24^{+0.01}_{-0.09}$	$130.1^{+3.6}_{-9.0}$	2^{+0}_{-1}	[1000]	444^{+6}_{-3}	
BCG	[0.0]	[0.0]	[0.20]	[34.0]	34^{+0}_{-5}	258^{+1}_{-12}	373^{+28}_{-7}	
GAL1	[3.2]	[− 11.1]	$0.02^{+0.01}_{-0.09}$	$94.3^{+6.7}_{-2.1}$	[0]	44^{+1}_{-3}	171^{+2}_{-10}	
L* galaxy					[0.15]	67^{+5}_{1}	143^{+1}_{-18}	

Table B5. Multiple images used for the models of MACS0329. The results on the redshifts estimation are the ones of model III.

ID	α (°)	δ (°)	$z_{\rm prior}$	$z_{\rm model}$
A.1	03:29:40.74	−02:13:17.90	1.112	
A.2	03:29:40.85	−02:13:17.19	1.112	
A.3	03:29:40.87	−02:13:17.44	1.112	
B.1	03:29:40.75	−02:13:18.15	1.112	
B.2	03:29:40.83	−02:13:17.17	1.112	
B.3	03:29:40.88	−02:13:17.93	1.112	
B.4	03:29:40.85	−02:13:18.54	1.112	
1.1	03:29:40.17	−02:11:45.71	6.18	
1.2	03:29:40.07	−02:11:51.71	6.18	
1.3	03:29:41.24	−02:12:04.66	6.18	
1.4	03:29:43.16	−02:11:17.36	6.18	
2.1	03:29:41.03	−02:11:29.06	2.14	
2.2	03:29:39.62	−02:12:00.66	2.14	
2.3	03:29:42.17	−02:11:25.61	2.14	
2.4	03:29:42.33	−02:11:54.46	2.14	
3.1	03:29:40.18	−02:11:26.56	[1.0-5.0]	$2.58^{+0.05}_{-0.05}$
3.2	03:29:39.06	−02:11:49.91		
3.3	03:29:41.26	−02:11:15.16		

Table B6. Parameters for the models of MACS0329.

Potential	$\Delta\alpha$ (arcsec)	$\Delta\delta$ (arcsec)	e	θ (°)	$r_{\rm core}$ (kpc)	$r_{\rm cut}$ (kpc)	σ_0 (km s^{-1})	γ
Model I								
GGL	[11.2]	[− 91.4]	[0.40]	[74.0]	[0]	[50]	209^{+1}_{-1}	
Model II								
GGL	[11.2]	[− 91.4]	[0.40]	[74.0]	[0]	[50]	196^{+2}_{-6}	
Ext Shear				$4.0^{+11.3}_{-2.1}$				$0.17^{+0.08}_{-0.04}$
Model III								
GGL	[11.2]	[− 91.4]	[0.40]	[74.0]	[0]	[50]	188^{+4}_{-9}	
DM1	$-1.4^{+0.4}_{-0.4}$	$-0.7^{+0.4}_{-0.2}$	$0.25^{+0.03}_{-0.01}$	$70.1^{+1.8}_{-2.7}$	58^{+19}_{-3}	[1000]	959^{+28}_{-19}	
DM2	$39.4^{+5.0}_{-1.8}$	$22.1^{+7.4}_{-2.0}$	$0.46^{+0.17}_{-0.10}$	$98.0^{+6.5}_{-6.0}$	119^{+0}_{-19}	[1000]	877^{+40}_{-38}	
BCG	[− 0.0]	[0.0]	[0.19]	[− 73.6]	[0]	[98]	208^{+11}_{-193}	
L* galaxy					[0.15]	[45]	155^{+6}_{-6}	
Model IV								
DM1	$-1.4^{+0.4}_{-0.4}$	$-0.7^{+0.4}_{-0.3}$	$0.24^{+0.03}_{-0.02}$	$69.4^{+1.8}_{-3.2}$	59^{+19}_{-4}	[1000]	984^{+24}_{-15}	
DM2	$38.2^{+5.4}_{-2.5}$	$20.7^{+8.6}_{-1.8}$	$0.48^{+0.16}_{-0.11}$	$98.3^{+2.2}_{-11.2}$	114^{+0}_{-12}	[1000]	833^{+37}_{-36}	
BCG	[− 0.0]	[0.0]	[0.19]	[− 73.6]	[0]	[98]	75^{+14}_{-242}	
L* galaxy					[0.15]	[45]	157^{+5}_{-7}	

This paper has been typeset from a TEX/LATEX file prepared by the author.